Modeling of surface nanostructures for sensorics

Master's Thesis

Alekszej Romanenko

Materials Science MSc.

Supervisor: Dr. Péter Petrik

MTA EK MFA

Internal advisor: Dr. Éva Kiss

ELTE, Department of Physical Chemistry

Eötvös Loránd University
Faculty of Science

Budapest, 2017

Acknowledgments

This thesis could not exist without the help of my supervisor, Dr. Péter Petrik. I thank Péter for his aid and guidance I received throughout this work. Our discussions always helped me and broadened my perspectives. I also thank him for always being available and for replying to every email promptly. I am very grateful to him most of all for his encouragement and enthusiasm. I am thankful for calling my attention to this topic. I also thank Prof. Éva Kiss for being my advisor and checking my thesis.

I would also like to acknowledge every member of the Ellipsometry research group in the MFA Photonics Laboratory, most of all Benjamin Kalas, for his help and support.

Finally, I want to express my gratitude to my family and friends for their support. Thank you all.

Contents

List of abbreviations

OWLS	waveguide lightmode spectroscopy
GCI	grating coupled interferometry
SE	spectroscopic ellipsometry
LRA	linear regression analysis
MSE	mean squared error
EMA	effective medium approximation
AFM	atomic force microscope
Fgn	fibrinogen
FF	flagellar filament
AOI	angle of incidence
MQ	milli-Q
PBS	phosphate-buffered saline
RSA	random sequential adsorption
SEM	scanning electron microscopy
ASF	available surface function

1 Preface

In the field of nanotechnology, one of the main directions is the realization and development of sensors or sensing systems that are able to detect even small amount ($\sim$ pg/ml) atoms with high temporal resolution. The investigation of such molecules typically requires a sensitive and specific method to detect them in a solution that contains large amount of other molecules as well.

The most common detection of the targeted molecule experiments is usually performed by labeling the molecules. After the labeling step, the system searches for the signal provided by the markers in the liquid or surface examined [1]. The main disadvantage of the labeling method is that it can influence the measurement results of the process being studied. For this reason, researchers are tending more and more towards non-marking applications in recent years.

The other very commonly used techniques are the optical waveguide-based sensors. By using this methods the attached layer on the sensor's surface can be detected very accurately [2, 3]. The surface of the substrate layer is often modified to bind specific templates. This procedure is therefore more suitable for quantitative determination.

Different molecules can be connected not only to a waveguide layer, but to many different sensing surfaces that can assist in quantitative and qualitative detection. One of the broad research areas is protein-based bio-nanotechnology. By exploiting their specific molecular recognition capabilities, biosensors can be developed for the task of detection is loaded by the proteins. By inserting the sensory chip covered by them into a measuring device equipped with liquid cells, the binding of target molecules can be measured *in situ* and label free [4, 5]. In this case, it is a benefit of using optical methods in the visible range, because the processes can be monitored with high sensitivity without any damage to the system under consideration or significantly interfering with the experiment.

During my diploma work, I was involved in coatable chips, to which various proteins were adsorbed *in situ* in flow cells. By using spectroscopic ellipsometry I examined the kinetics of adsorption. The obtained surfaces were studied with different techniques. Since the measurements were complex, the creation and evaluation of optical models were required. By doing so, my main aspiration was to create a well usable biosensor.

2 Theory

2.1 Biosensors

Nowadays there are already many biosensor tools available, but their development is becoming more and more important. Reduction of their size and increase in their sensitivity, stability and specificity are another challenge for researchers and industry. Market enforcement of tiny, cheap and reliable tools is the desire of the humanity to make our lives comfortable in a variety of areas. For example the blood glucose monitoring devices that help ensure safe insulin delivery for diabetics [6].

Biosensor technology is based on target specific recognition of small amounts of molecules and biomolecules. One of the most important and main criterions for biosensor is that the target molecules, even if they are in low concentrations in the test solution, can bind to identifying elements but other molecules can not.

The general biosensor consists of a recognizer and a signal transducer unit. Selectiveness for a specific ligand is achieved by selective molecules immobilized on the surface of the sensor chip. The recognizing molecules can be antibodies, enzymes, receptors and even nucleic acids. The role of the signaling element is to transform recognition of the target molecules into the form of signal that can be evaluated. The transducer can also operate on acoustic, electrochemical, optical, piezoelectric and thermal principles. One of the most common methods is the usage of optical biosensors (Fig. 1).

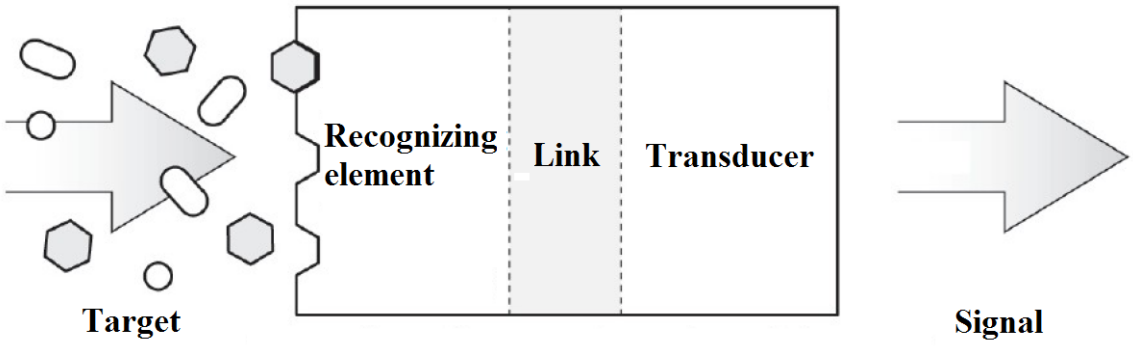

Figure 1: The examined target molecule is detected by the recognition element, and the effect of this is transformed by the transducer into a signal [6].

In order to reproduce the immobilization of the recognition elements on a surface of a sensor chip, it is essential to know the structure, stability, adsorption kinetics and surface orientation of these elements. Detailed knowledge of the adsorption processes of proteins is essential for biosensor development. Due to the differences in the proteins (size, shape, etc.), the kinetics of the surface immobilization of the proteins, the morphology and stability of the adsorbed layer may be different. Numerous non-marking methods are also available for the adsorption of proteins. Such as optical waveguide lightmode spectroscopy (OWLS) [7, 8], grating coupled interferometry (GCI) [9, 10], or ellipsometry [11, 12].

2.2 Basics of ellipsometry

Ellipsometry is a non-destructive optical measurement technique used to determine the thickness and dielectric properties of thin films (even with thickness of some nm or less). It can be used to test all properties that can be related to the optical response of the sample (e.g., surface roughness, complex refractive index). This method is not suitable for media with inhomogeneities with a larger size than the wavelength used. For example, samples with high surface roughness or greater than micron (usually they seem to be glance). This technique is indirect, so the relevant information can be obtained from model analysis. The unknown parameters in the model are systematically changed until the result based on the model gives the best match with the measured data.

2.2.1 Physical background

Ellipsometry measures the change of the light's polarization state caused by the interaction with the material of the investigated sample. Polarization is one of the light's properties. It can be described by the electric field **E** components [14]. The most common state of the polarization is elliptic (Fig. 2). When the beam is spreading in the z direction the electric field z component is zero because the light is a transversal wave. In this case, the E_x and E_y components are:

$$\mathbf{E}(z,t) = \begin{bmatrix} E_x\,(z,t) \\ E_y(z,t) \end{bmatrix} = \begin{bmatrix} a_x\, e^{i(\frac{\mathbf{n}}{c}z - wt + \delta_x)} \\ a_y\, e^{i(\frac{\mathbf{n}}{c}z - wt + \delta_y)} \end{bmatrix} = \mathbf{A}\, e^{i(kz-wt)}, \tag{1}$$

where w is the angular frequency, δ_n is the phase, $n = N - ik$ is the complex refractive index, and c is the speed of the light in vacuum. $\mathbf{A}$ is the Jones vector witch describes the polarization of the light:

$$\mathbf{A} = \begin{bmatrix} A_x \\ A_y \end{bmatrix} = \begin{bmatrix} a_x\, e^{i\delta_x} \\ a_y\, e^{i\delta_y} \end{bmatrix} \tag{2}$$

There are different polarization changing devices they can be described by the well known Jones matrix ($\mathbf{J}$). The change from an $\mathbf{A}$ to an $\mathbf{A}^*$ polarization state look like:

$$\mathbf{A}^* = \mathbf{J} \cdot \mathbf{A}. \tag{3}$$

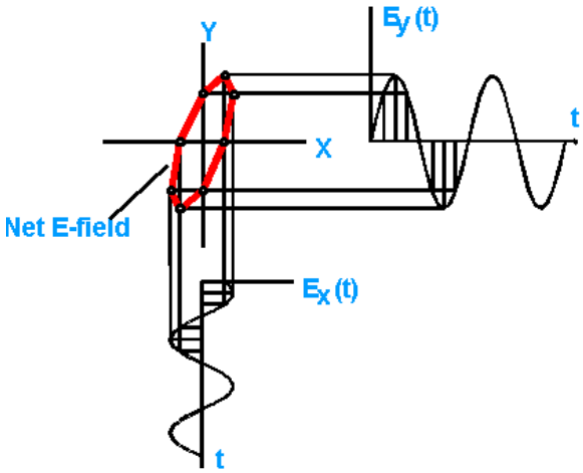

Figure 2: Elliptically polarized light [13].

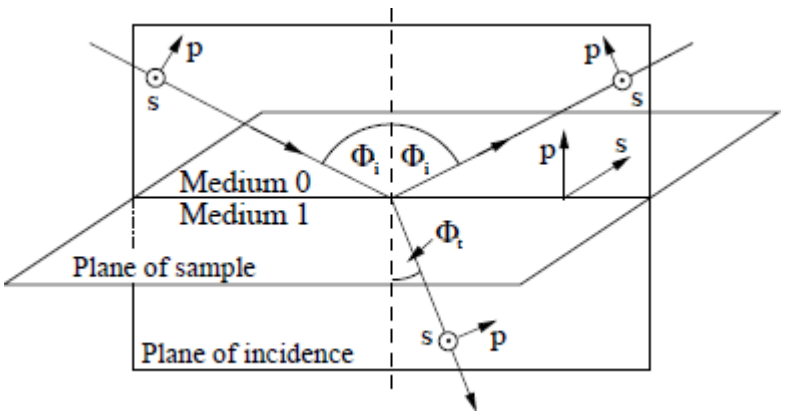

Figure 3: Reflexion of polarized light [15].

Reflection and transmission of the light (Fig. 3) can also be examined with the Jones matrix formalism. The state of polarization can be described by dividing the light beam into two parts that are perpendicular (E_s) and parallel (E_p) to the plane of incidence (both denotes complex values). Both components are plane waves described in Ref. [16]. If we use the Maxwell equations and apply the boundary conditions on them we can get the Fresnel reflection and transmission coefficients.
TM - parallel case:

$$r_p = \frac{n_2 cos\Phi_i - n_1 cos\Phi_t}{n_1 cos\Phi_t + n_2 cos\Phi_i}\,, \tag{4}$$

$$t_p = \frac{2n_1 cos\Phi_i}{n_1 cos\Phi_t + n_2 cos\Phi_i}. \tag{5}$$

TE - perpendicular case:

$$r_s = \frac{n_1 cos\Phi_i - n_2 cos\Phi_t}{n_1 cos\Phi_i + n_2 cos\Phi_t} = t_s - 1\,, \tag{6}$$

$$t_s = \frac{2n_1 cos\Phi_i}{n_2 cos\Phi_i + n_1 cos\Phi_t} = r_s + 1\,. \tag{7}$$

,
where Φ_i is the angle of incidence, the reflected angle and Φ_t is the transmitted angle. The reflection coefficients can be negative but the transmitted ones are always positive.

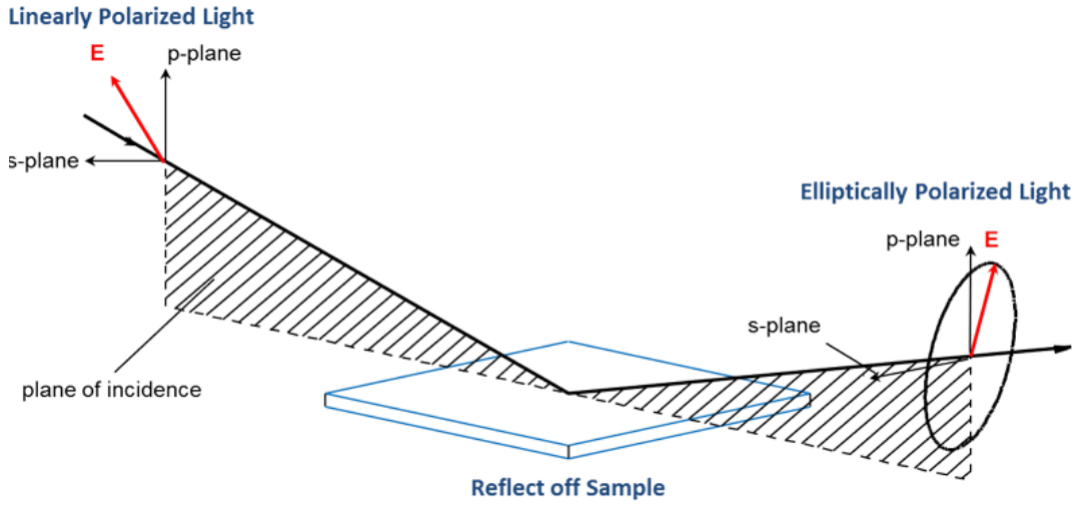

Figure 4: Reflection of a linear polarized wave [13].

If polarized light is reflected from the boundary of two media, the state of polarization of the reflected light beam will be elliptic, circular, or even linear depending on the sample's characteristics (Fig. 4). As it was mentioned before, with spectroscopic ellipsometer we can measure this changes in the polarization [14]. The special features of method are its high speed, high sensitivity and the non-destructive nature that makes it capable for *in situ* monitoring of biological processes [17]. With it we can measure the wavelength dependence of the dielectric function. Our aim in the measurements is to determine the thickness and dielectric properties of the layers.

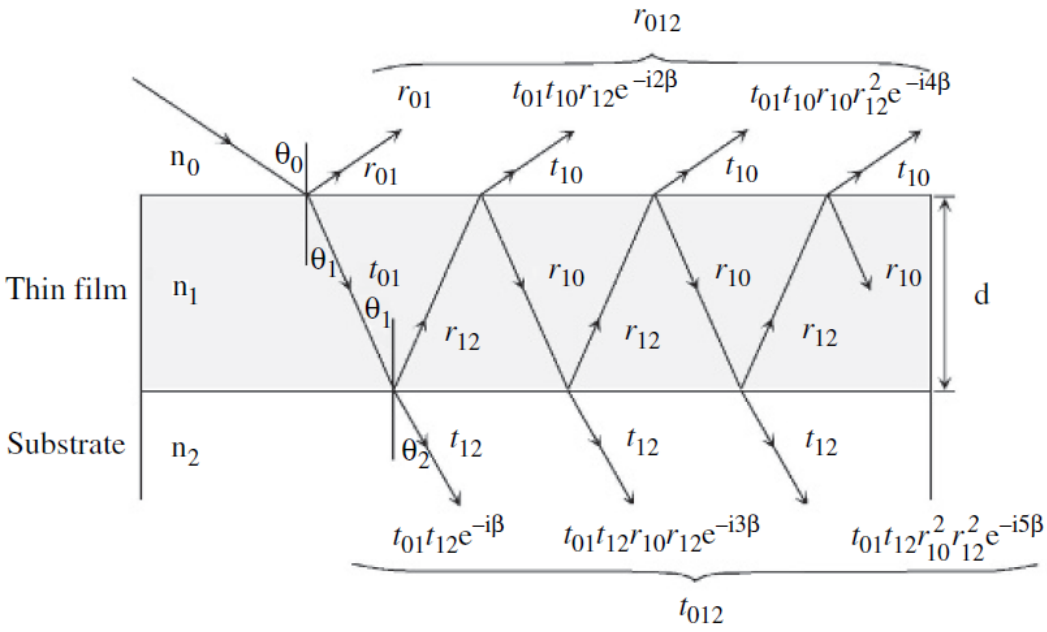

Figure 5: Light has multiple reflections and transmissions in the thin layer, in the case of a three-medium system [15].

So how to get the information about the samples thickness and the dielectric properties? To learn this information an optical model for an ambient/thin film/substrate structure with 3 media (Fig. 5). The amplitude reflection coefficient for this substrate structure is expressed from the sum of all the reflected waves (all of the r_n and t_n coefficients have a p and s components):

$$r_{012} = r_{01} + t_{01}t_{10}r_{12}e^{-i2\beta} + t_{01}t_{10}r_{10}r_{12}^2e^{-i4\beta} + t_{01}t_{10}r_{10}^2r_{12}^3e^{-i6\beta} + ... \tag{8}$$

Here β denotes is the the phase variation and it's called the film phase thickness.

$$\beta = \frac{2\pi d}{\lambda} n_1 cos\theta = \frac{2\pi d}{\lambda}(n_1^2 - n_0^2 sin^2\theta)^{1/2}. \tag{9}$$

d and n_i are the thickness and the refractive index of the medium. Since the infinite series $y = c + cr + cr^2 + cr^3 + ...$ can be reduced to $y = c/(1-r)$, we get:

$$r_{012} = r_{01} + \frac{t_{01}t_{10}r_{12}e^{-i2\beta}}{1 - r_{10}r_{12}e^{-i2\beta}}\,. \tag{10}$$

There are the relations expressed by:

$$r_{01} = -r_{10}\,, \tag{11}$$

$$t_{01}t_{10} = 1 - r_{01}^2\,. \tag{12}$$

If we apply these to (10), we obtain the familiar form:

$$r_{012} = \frac{r_{01} + r_{12}e^{-i2\beta}}{1 + r_{01}r_{12}e^{-i2\beta}}\,. \tag{13}$$

Similarly, the amplitude transmission coefficient t_{012} can be given.

As I mentioned above all of the r_n and t_n coefficients have a p and s components. If we look at the fraction of the r_{012} p and s components we get the ellipsometry main equation:

$$\frac{\bar{r}_p}{\bar{r}_s} = tan\Psi e^{i\Delta} = \bar{\rho}\,. \tag{14}$$

Paul Drude [18, 19] introduced this terminology of the $\bar{\rho}$ witch is called the complex reflectance ratio. The values Ψ and Δ are called the ellipsometric angles.

The state of polarization of a plane wave is defined by

$$\bar{\chi} = \frac{E_p}{E_s}. \tag{15}$$

where $\bar{\chi}$ is called the polarization coefficient. An ellipsometric measurement provides the ratio of the polarization coefficients of the reflected ($\bar{\chi_r}$) and incident ($\bar{\chi_i}$) light:

$$\bar{\rho} = \frac{\bar{\chi_r}}{\bar{\chi_i}}\,; \tag{16}$$

combining the Eq. (14) - (16) we get the following equation:

$$\bar{\rho} = \frac{\bar{\chi_r}}{\bar{\chi_i}} = \frac{|\bar{\chi_r}|}{|\bar{\chi_i}|} e^{i(\delta_r - \delta_i)} = tan\Psi e^{i\Delta}. \tag{17}$$

The ratio of the polarization coefficients is equivalent with the ratio of the Fresnel refection coefficients $\bar{r}_p$ and $\bar{r}_s$:

$$\frac{\bar{\chi_r}}{\bar{\chi_i}} = \frac{\frac{E_r,p}{E_r,s}}{\frac{E_i,p}{E_i,s}} = \frac{\bar{r}_p}{\bar{r}_s}. \tag{18}$$

The ellipsometric angles can be written as

$$tan\Psi = \frac{|\bar{r}_p|}{|\bar{r}_s|} = \frac{|\bar{\chi_r}|}{|\bar{\chi_i}|}, \tag{19}$$

and

$$\Delta = \Delta_p - \Delta_s = \delta_r - \delta_i \,, \tag{20}$$

where δ denotes the phase of the components (i - incident, r - reflected). $Tan\Psi$ is the ratio of the absolute values of the reflected and incident polarization components.

During the measurement the wavelength dependence of the Ψ and Δ can be directly determined. The thickness of the thin layer and its refractive index are the expression of β. Since $\bar{\rho}$ can be written as a function of β but Ψ and Δ do not contain analytically d and n_1 that is why optical model construction needed to get the layer physical characteristics.

2.2.2 Spectroscopic ellipsometer set-up

Before moving on to optical models I would like to present our measuring set-up. Since the start of my work at Institute of Technical Physics and Materials Science I have been working with a *Woollam* M2000DI spectroscopic ellipsometer (SE) (Fig. 6). Every ellipsometer is basically an optical instrument that consists of two arms, whose axes lie in the same plane. In our case we have two light sources: the visible and the infrared parts of the spectrum is supported by a halogen lamp, the UV part is supported by a deuterium lamp. As a result, we have a wide wavelength range from 170 nm to 1690 nm. The ellipsometer's other main parts are the polarizer,

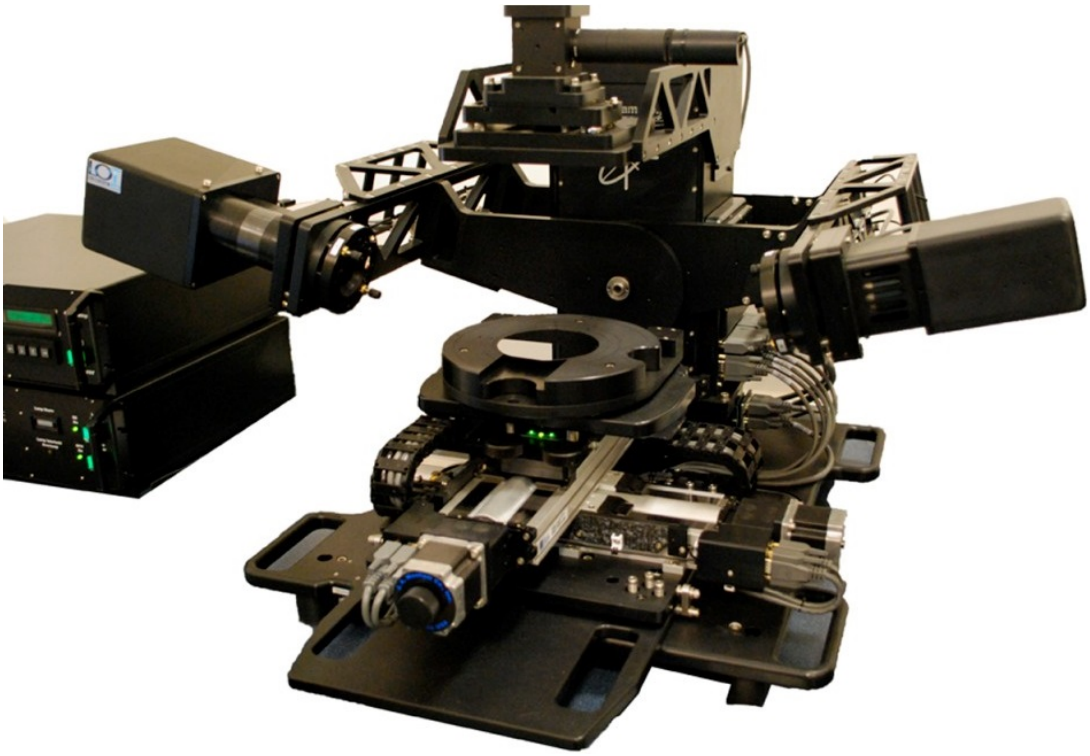

Figure 6: *Woollam* M2000DI spectroscopic ellipsometer.

compensator (modulates the phase of the light beam), sample, analyzer and of course the detector. The polarizer-compensator combination operates as a general elliptical polarizer.

Hereinafter, I describe the operation of a rotary-analyzer ellipsometer since the rotating-compensator ellipsometer is much more complex. The light passing through the polarizer becomes linearly polarized, then the sample reflects it, the polarization state of the wave changes and becomes elliptically polarized generally. The instrument also includes automatic goniometer and sample stage as well as an electronic control and processing unit. Different polarization directions are scanned in time by the rotating analyzer. The reflected elliptically polarized light is scanned by letting trough different orientations of the ellipse. So the signal that appears on the detector will be a periodic (sinusoidal) function of time (Fig. 7) and it's Fourier transform:

$$I = I_0 \left[\alpha(A) cos\, 2P + \beta(A) sin\, 2P + 1\right], \tag{21}$$

where A and P are the azimuthal angles of the analyzer and the polarizer, I is the intensity we got on the detector and α and β are the double-frequency Fourier coef-

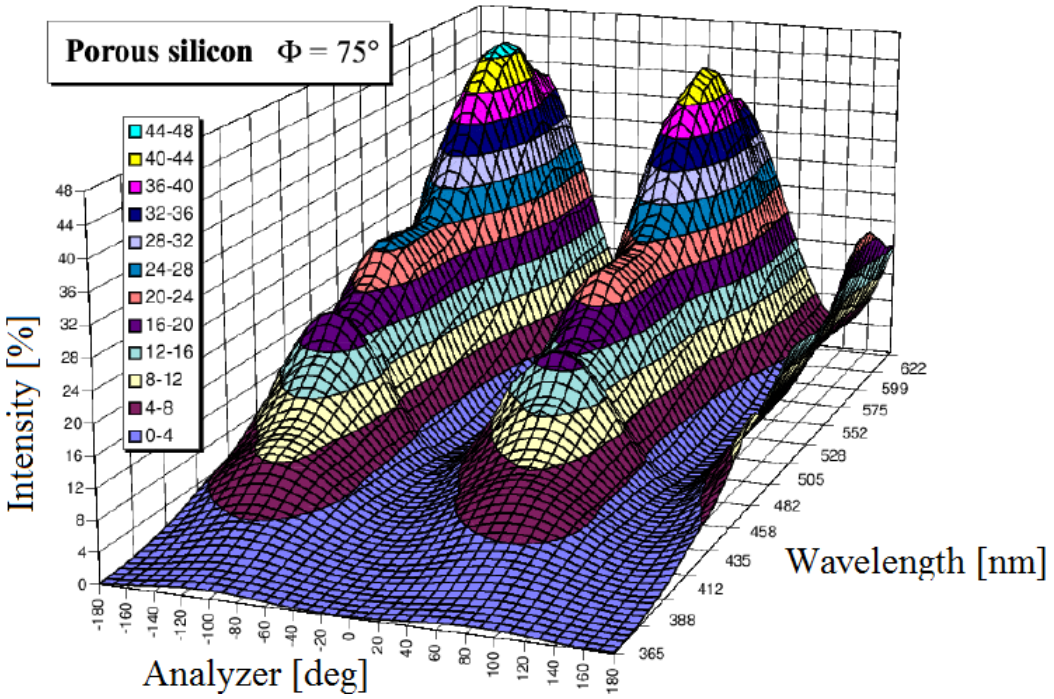

Figure 7: Detector signal at a rotating analyzer or polarizer ellipsometer as a function of the azimuthal angle of the rotating component.

ficients. This equation shows that the zeroth and second harmonics in the Fourier-transform of the signal I contains all the information needed for the determination of the complex reflectance ratio $\bar{\rho}$.

To get the ellipsometric angles $tan(\Psi)$ and $cos(\Delta)$ using α and β, one needs to express intensity as a function of the azimuthal angles of the polarizer and the analyzer, and as a function of the reflection coefficients of the reflected wave. The optical components at the detector can be written as the sequential application of the polarization devices mentioned above each one of the Jones matrices:

$$\underset{Detector}{\begin{bmatrix} E_{d,p} \\ E_{d,s} \end{bmatrix}} = \underset{Analyzer}{\begin{bmatrix} 1 & 0 \\ 0 & 0 \end{bmatrix}} \underset{Rotation}{\begin{bmatrix} cos\,A & sin\,A \\ -sin\,A & cos\,A \end{bmatrix}} \underset{Sample}{\begin{bmatrix} \bar{r}_p & 0 \\ 0 & \bar{r}_s \end{bmatrix}} \underset{Rotation}{\begin{bmatrix} cos\,P & -sin\,P \\ sin\,P & cos\,P \end{bmatrix}} \underset{Polarizer}{\begin{bmatrix} 1 & 0 \\ 0 & 0 \end{bmatrix}} \underset{Source}{\begin{bmatrix} E_p \\ E_s \end{bmatrix}}. \quad (22)$$

The light intensity in the detector is the sum of the squares of the absolute amplitudes:

$$I = |\bar{E}_d|^2 = |\bar{E}_{d,p}|^2 + |\bar{E}_{d,s}|^2. \quad (23)$$

The product of the multiplications in Eq. (22):

$$\begin{aligned} I = [\,|\bar{r}_p|^2\, cos^2 A\, cos^2 P + |\bar{r}_s|^2\, sin^2 A\, sin^2 P + \\ + (\bar{r}_p \bar{r}_s^* + \bar{r}_p^* \bar{r}_s)\; cos\, A\, sin\, A\, cos\, P\, sin\, P\,]|\bar{E}_0|^2. \end{aligned} \tag{24}$$

After linearization and comparison with Eq. (21), α and β can be calculated as:

$$\alpha = \frac{tan^2\,\Psi - tan^2\, A}{tan^2\,\Psi + tan^2\, A}\,, \tag{25}$$

$$\beta = 2cos\,\Delta\, \frac{tan\,\Psi\, tan\, A}{tan^2\,\Psi + tan^2\, A}. \tag{26}$$

From these equations $tan\,\Psi$ and $cos\,\Delta$ can be expressed as:

$$tan\,\Psi = |tan\, A| \sqrt{\frac{1+\alpha}{1-\alpha}}\,, \tag{27}$$

$$cos\,\Delta = sign\,(tan\, A) \frac{\beta}{\sqrt{1-\alpha^2}}. \tag{28}$$

2.3 Optical models

To get valuable information, we first need a proper optical model. Thus we can measure a sample of completely unknown components by an ellipsometer. To determine the unknown parameters one has to increase the amount of independent information. There are several possibilities, e.g. multiple angles of incidence, and different layer thickness of the same material. The most important is the multi-wavelength SE.

As it was mentioned before we get a characteristic spectrum (Ψ and Δ values depending on the wavelength), but only by looking on this dataset, mostly we cannot say much about the structure. At least we approximately need to know the material quality and the microstructure of the layers contained in the examined sample, which can be used to build an optical model. Knowledge of material quality includes knowledge of the reference refractive index of ingredients, which is not a requirement at all. Because the wavelength dependence of the refractive index can be parameterized using an analytical models.

Next step is to identify unknown parameters in the suspected model such as layer thickness or porosity. This can be done with a suitable driver. During my work, I used the *CompleteEASE* and *WVase* software specially designed for ellipsometric calculations for the *Woollam* M2000DI ellipsometer. These and other programs are made to find the parameter values using the linear regression analysis (LRA) technique to minimize the differences between the calculated and experimental data by adjusting the model parameters, and finally to obtain the results in terms of best-fit model parameters and their confidence limits, as well as the smallest of the mean squared error (MSE) for a particular model and spectrum.

The following is the equation for MSE:

$$MSE = \sqrt{\frac{1}{2N-M}\sum_{j=1}^{N}\left\{\left(\frac{\Psi_j^{meas}-\Psi_j^{model}}{\sigma_\Psi^{meas}}\right)^2+\left(\frac{\Delta_j^{meas}-\Delta_j^{model}}{\sigma_\Delta^{meas}}\right)^2\right\}}, \quad (29)$$

where N is the number of independent readings corresponding to the different wavelengths at which SE measurements are made, M is the number of unknown model parameters, Ψ^{meas} and Δ^{meas} are measured, Ψ^{model} and Δ^{model} are the ellipsometric angles calculated on the basis of the model; σ^{meas} is the deviation of the measurement of the ellipsometric angles. Each period of the compensator rotation is a measurement.

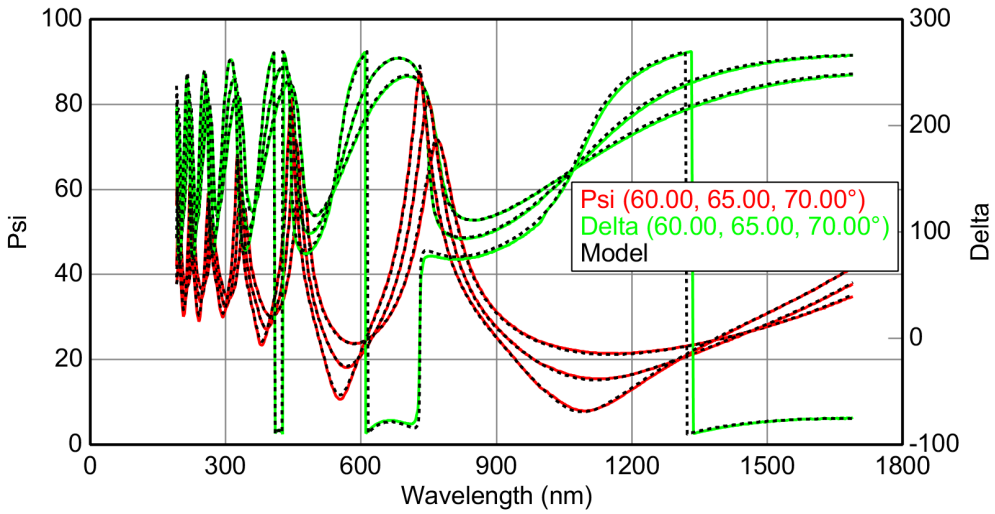

Figure 8: SE spectrum (red and green lines) and fitted model (broken black line) of 490 nm thick thermal oxide silicon layer.

The MSE value provides information on the quality of the fit. With this, it is decidable, for example, which one of the two alternative models describes better the reality. In addition, we can conclude from the error of parameters obtained from the fitting the correlation between the parameters. Fig. 8 shows a typical measured spectrum and a matched curve according to a suitable model.

In the course of the evaluation, I used reference refractive indexes for Si and thermal SiO_2 known from the literature. It is not easy to determine the refractive indexes because we would like to get them as the functions of the wavelength (Fig. 9). During my work I mostly used two models: Cauchy's dispersion Eq. 30 and the effective medium theory to determine the optical properties of the investigated structures.

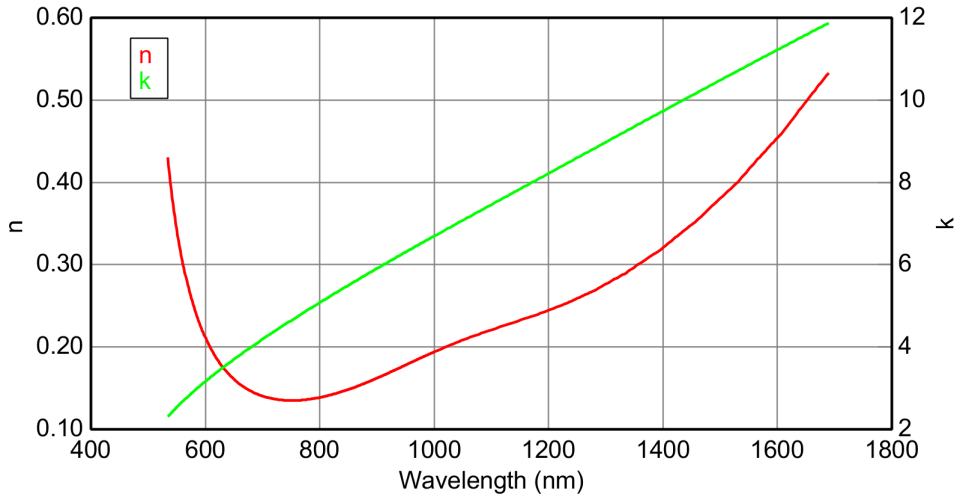

Figure 9: Optical constants of Au.

2.3.1 Cauchy's dispersion equation

The most common usage of the *Cauchy formula* is the description of the optical properties of dielectrics. In this case the refractive index of a layer without a reference value of the sample can be given by a reciprocal function of the wavelength. According to the *Lorentz*'s theory the refractive index of the investigated material is characterized by a refractive index of the sum of independent linear oscillators. Cauchy used this method and the result of this approach is the following dispersion formula:

$$n(\lambda) = A + \frac{B}{\lambda^2} + \frac{C}{\lambda^4} + \cdots, \tag{30}$$

where parameter A is the wavelength independent part of the refractive index, and the B and C coefficients represent the dispersion. In the most cases, it is enough to use the first and second coefficients, the third term is often negligible because it does not always mean a more accurate result.

2.3.2 Effective medium theory

There are different effective medium approximations (EMA) and the main goal of them is to determine the dielectric function of macroscopically homogeneous and microscopically heterogeneous or even composite materials [11]. Other examples include polycrystalline films, amorphous materials and glasses. A microscopically rough surface can also be considered as a heterogeneous, being a mixture of bulk and ambient on a microscopic scale. The material is considered as macroscopically homogeneous, if the phases are smaller than the wavelength of the light beam.

That is why the basic assumption of the effective medium theory is that, if the inhomogeneity is so small, that the change is negligible in the macroscopic electromagnetic field induced by incident light which results from scattering and deflection on heterogeneities. It is assumed that each component has a refractive index equal (or proximate) to the optical densities of the bulk materials. The model can be used to give a good approximation of conductivity (σ) as well as the dielectric function ($\bar{\epsilon}$). The relationship between the refractive index and the dielectric constant is given by the following equation:

$$\bar{n}\left(\omega\right) = \sqrt{\bar{\epsilon}\left(\omega\right)}\,. \tag{31}$$

Approximation considers the layer as a mixture of two materials with different optical properties.. The two materials are indicated as X and Y, where the dielectric functions of the X, Y complexes are $\epsilon_x\left(\omega\right)$, $\epsilon_y\left(\omega\right)$ and the volume ratios are r and $(1-r)$, respectively. The dielectric functions can be written as:

$$\epsilon_j\left(\omega\right) = \epsilon_{j\,b}\left(\omega\right) + \frac{4\pi i\,\sigma_j\left(\omega\right)}{\omega}\,, \tag{32}$$

where $j = x, y$; $\epsilon_{j\,b}\left(\omega\right)$ represents the contribution of the dipole moment to the dielectric, and $\sigma_j\left(\omega\right)$ is the conductivity.

Two vectors are used to characterize the electrical space: the electric field **E** and the **D** electric displacement field. These two vectors are not independent of each other. The relationship between them depends on the material characteristics that fills the space. The following relationship applies in isotropic media:

$$\mathbf{D} = \epsilon_i \, \mathbf{E} + \mathbf{P}. \tag{33}$$

The mathematical background of the effective medium approximation is the following: first, at each point of the given microstructure, the local dipole moments and the electrical field strengths are exactly determined. Second, averaging them, we get their macroscopic equivalents - **E** and **P** polarization vectors. Further, the following relationship is known:

$$\mathbf{D} = \epsilon_0 \, \mathbf{E} + \mathbf{P}. \tag{34}$$

Based on the considerations so far, we can get the $Clausius-Mosotti$ equation:

$$P_m = \frac{\epsilon_r - 1}{\epsilon_r + 2} \cdot \frac{M}{\rho} = \frac{1}{3} \, N_A \bar{\alpha} \, , \tag{35}$$

where M is the molar mass of the dielectric material, ρ is its density, $\bar{\alpha}$ is the polarizability of the molecule, and N_A is the $Avogadro$ constant. The quantity P_m is called molar polarization. Further considerations are needed [20] to get a final term that can be used in the case when the volumes of the two materials X, Y are comparable in the investigated area. This form of the approximation is called the $Bruggeman$ equation:

$$r \frac{\epsilon_x - \epsilon_{eff}}{\epsilon_x + 2\epsilon_{eff}} + (1 - r) \frac{\epsilon_y - \epsilon_{eff}}{\epsilon_y + 2\epsilon_{eff}} = 0. \tag{36}$$

This expression contains the effective dielectric function. By using the relation given by Eq.(31), the effective refractive index can be attributed to the whole layer (X, Y).

2.3.3 De Feijter equation

Surface adsorption of the proteins can be characterized by surface adsorbed mass densities, which is the protein mass on the unit surface of the substrate. According to *de Feijter*'s [21] article, this quantity can be written in the following form:

$$\Gamma = \int_0^\infty \Delta c(z)\ dz\,, \tag{37}$$

where z is the direction perpendicular to the surface of the layer. $c_1(z)$ is the absolute concentration in the layer and c_2 is the solute concentration in the bulk solution ($z \to \infty$), so $\Delta c\,(z) = c_1(z) - c_2$ is the excess concentration of the solute in the adsorbed layer (mass per volume unit) [22]. If the correlation between the refractive index and the concentration of the solution is linear, then the surface mass density using the average thickness H and the average refractive index $\bar{n}_1$ of the layer:

$$\Gamma = \frac{H(\bar{n}_1 - n_2)}{dn/dc}. \tag{38}$$

The *de Feijter*'s equation most commonly used form is:

$$\Gamma = \frac{h(n - n_0)}{dn/dc}\,, \tag{39}$$

where n is the refractive index of the protein, n_0 is the refractive index of the medium (usually the buffer solution), h is the thickness of the protein layer, and dn/dc is the refractive index increment. In several proteins this value was found to be equal to: 0.182 cm^3/g (at 633 nm wavelength) [21]. The formula is valid in the concentration range where the refractive index is a linear function of the concentration. According to *de Feijter*'s work, we know that this assumption is valid for protein solutions at a concentration below 0.4 g/ml.

If the spectra of [$\Psi(\lambda)$, $\Delta(\lambda)$] were measured *in situ* and it is given within a time period, due to the adsorption the change in thickness and in refractive index [$h_a(t)$, $n_a(\lambda, t)$] can be determined over a time period. Then, by using this information, we can get the $\Gamma(t)$ function by using Eq. (39).

2.4 Atomic force microscopy

The principle of the atomic force microscope (AFM) is based on recording the force interaction between the surface of the sample and the probe. The sample is mapped by detecting this interaction point by point. As a probe, a nanosized tip is used (having a radius of just a few nm), located at the end of an elastic, thin ($\sim$ 1mm) cantilever. The force acting on the probe from the side of the surface leads to the bending of the console. The appearance of elevations or depressions under the tip leads to a change in the force acting on the probe, and hence, the change in the magnitude of the cantilever's bending. Thus, by recording the value of the bend, one can draw a conclusion about the relief of the surface. However, the repulsion force between the surface and the needle is not measured directly, but based on the reflection of a laser beam from the console (Fig. 10). The AFM resolution is $\times$1000 better than the optical diffraction limit. However, due to the convolution, the lateral resolution ($\sim$ 30 nm) is lower than the vertical resolution, which can be 0.1 nm.

The most important forces acting between the probe and the sample are, first of all, the long-range *van der Waals*, which are the forces of attraction, but in the course of their further approach they become repulsive forces. Three operating modes of the atomic force microscope are distinguished:

- Contact mode
- Semi-contact mode or tapping mode
- Non-contact mode

When studying biological samples, it is worth working in non-contact mode, since in contact mode, a needle by contacting the proteins, cells, and other objects may violate the pattern. In non-contact mode, the needle oscillates from the pattern at a distance that the force between the surface and the tip ($\sim$ pN magnitude) is in the attracting range. In this case, the needle is close enough to the sample, but it does not affect it.

The piezoelectric vibrator is excited with oscillations of the probe at a certain frequency (near to the resonance frequency). The force acting on the surface side leads to a shift in the amplitude-frequency and phase-frequency characteristics of the probe, and the amplitude and phase of the vibration change values. The feedback

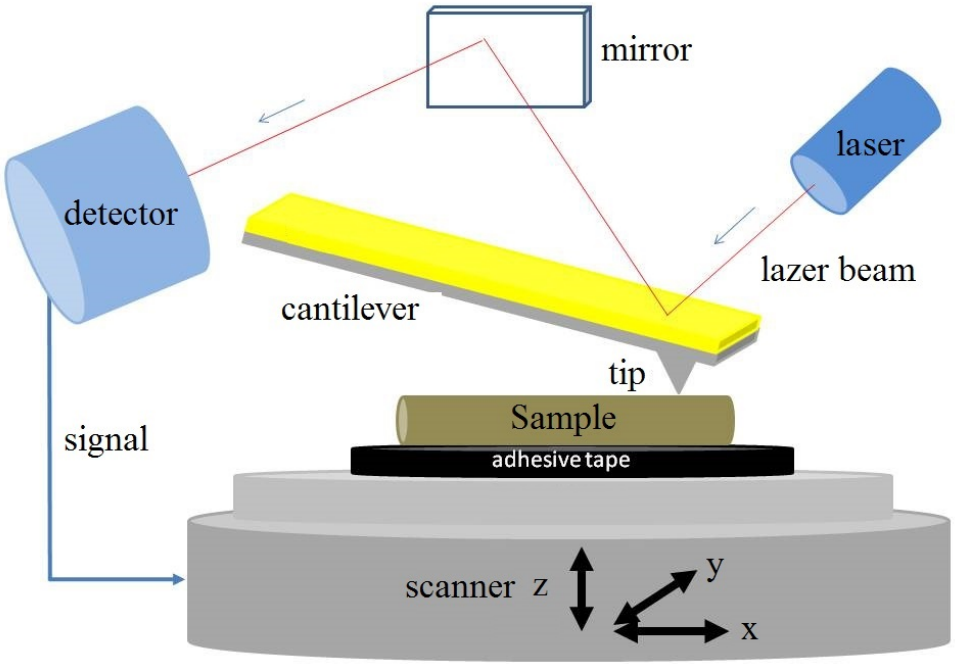

Figure 10: Schematic of an atomic force microscope with optical detection of the deflection of the cantilever [22].

system, as a rule, maintains a constant amplitude of the probe's oscillations, and the change in frequency and phase at each point is recorded. However, it is possible to establish feedback by maintaining a constant value of the frequency or phase of the oscillations. The disadvantages of the method is low scan speed. We used AFM to study the morphology of the adsorbed proteins. The measurements will be discussed in more details later in section 4.6.

2.5 Fibrinogen

Parts of my measurements were performed with fibrinogen (Fgn). It is a protein in the bloodstream that occurs in all vertebrate's blood. It is estimated that the plasma may contain $\sim$40,000 different proteins. The Fgn takes approximately 3% of plasma, the normal amount is 200–450 mg/100 ml . The liver synthesizes this protein with a molecular weight of 340 kDa and an isoelectric point of 5.8. It consists of three polypeptide chains - domains (Fig. 11a). Fibrinogen plays an important role in our blood clotting.

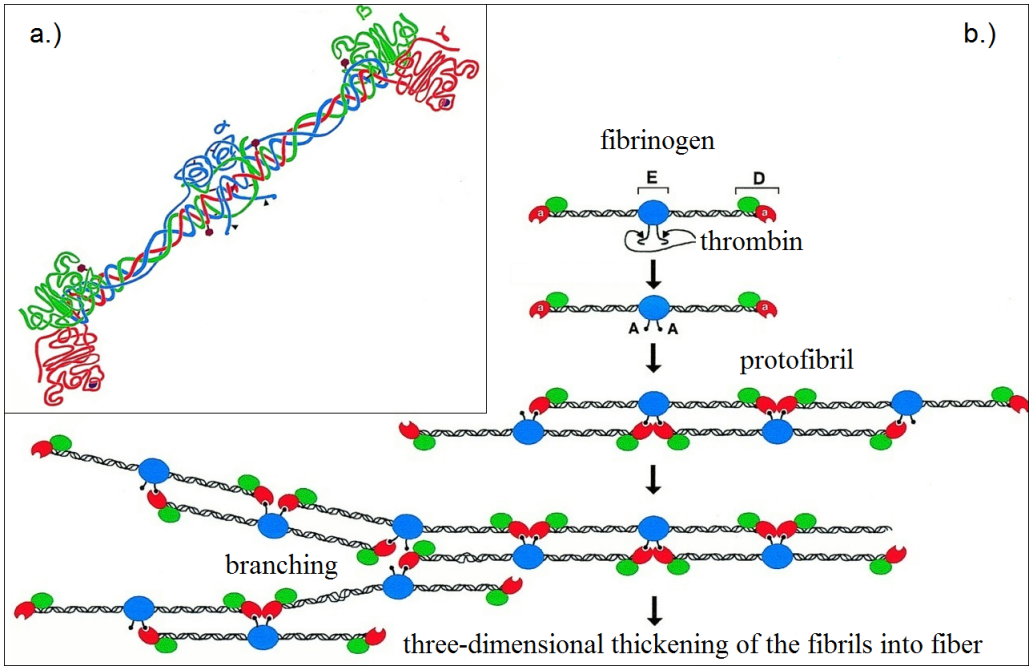

Figure 11: Schematic representation of human fibrinogen. The α chain is shown in blue, the β chain in green, and the γ chain in red [25].

By the catalytic action of thrombin enzyme, the fibrinogen polymerizes, becomes fibrin and it is insoluble in water (Fig. 11b) [23]. The mesh of the fibrin and the cellular elements collapse at the injured section. Blood clotting is an important process, but it is a problem in artificial interventions, because the proteins of the plasma are imparted to the organs and the surgical instruments immediately [24]. That is how fibrinogen increases the adhesion of bacteria, and the implant becomes infected.

To study the surface interaction of proteins and biomaterials, fibrinogen is a suitable model protein, because it is large enough for its phenomena to be perceived, but its structure is not so complex that it can not be described with a simple optical model. Fibrinogen can be adsorbed on almost any surface with and without any prior chemical surface treatment. However, by the appropriate chemical process, the binding of protein molecules can be facilitated.

Fgn's simple structure and smaller size makes it a good model protein for the measurements. Its adsorption is published in the literature [26], and it is therefore a good reference to understanding a more complex structure such as the adsorbed flagellar filament layer.

2.6 Flagellar filaments

2.6.1 Structure of flagellar filaments

Flagellar filaments (FFs) are self-organizing supramolecular systems. They are the extracellular parts of bacterial movement organs (flagellas) (Fig.12a). Understanding the properties of macromolecular systems capable of self-organizing, actively responding to environmental changes is crucial and important. Many researchers tried to find out are the backgrounds of the self-organizing ability of flagellar proteins.

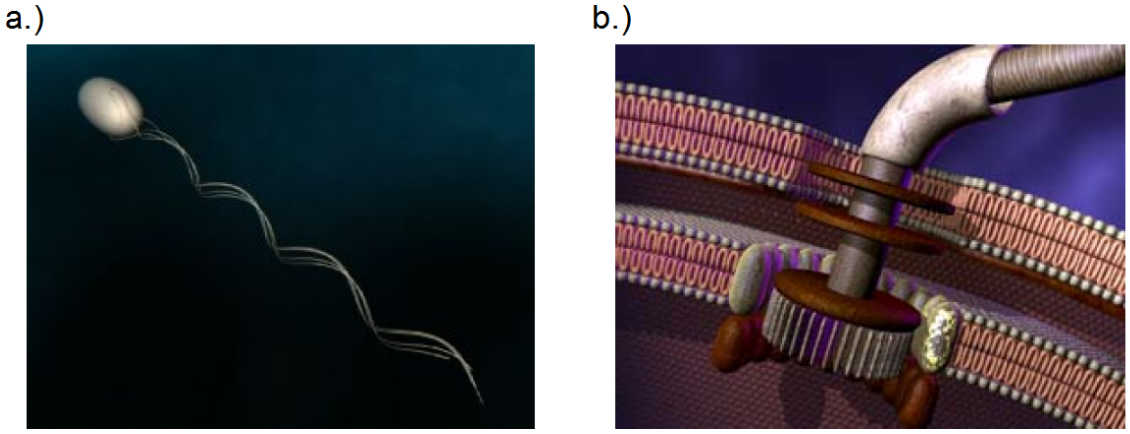

Figure 12: a.) Helically organized from the cell membrane of the bacterium, several micrometers long FFs; b.) a schematic drawing of a filament driving motor [29].

Each filament is driven by a 50 nm wide rotating engine in the cell membrane (Fig. 12b), the speed of which can reach the unbelievably large revolution of up to ninety thousand per minute [27, 28]. The energy of the rotation is provided by ATP gradient. The FFs are bound to a binder and propagate the bacteria with a coordinated motion at a rate of $\sim$ 25 μm/s. The motor shaft is connected to the filament by hooks. This hooks are attached to the protein wrap by HAP1 and HAP3 proteins.

The engine's axis of building proteins, as well as hook proteins, flagellins and HAP proteins are commonly referred to as axial proteins. These are synthesized in the cytoplasm and then through the tubular structure of the filament they reach their insertion site at the end of the filaments [30]. The end is terminated by a cap-like formation consisting of a few copies of the HAP2 protein.

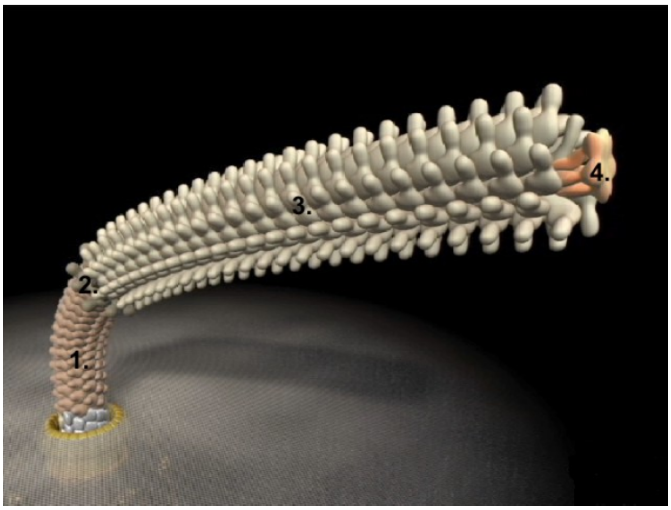

Figure 13: Structure of flagellar filament: 1. Hook 2. HAP1, HAP3 3. Flagellin subunits 4. HAP2 cap [29].

This cap allows the flagellin subunits to transpose through the filament to incorporate into the end of the filaments and not to diffuse into the medium. It is very tightly bound to the end of the filaments. However, it is able to locally release the end of the filaments at a convenient moment, allowing the incorporation of new arriving flagellin subunits. This way HAP2 regulates the attachment of the arriving subunits and protects the filament from any depolymerization (Fig. 13).

The filament builds up step-by-step from the bacterial cells. During the flagellum formation, the growing filament flagellin (51480 Da) monomers are polymerized [31]. During the polymerization, the monomers are helically organized into filaments. The smallest repeating unit of the helical filament consists of two threads, built up from 11 flagellins (Fig. 14b). FFs have a diameter of 23 nm and their length typically ranges from 5 μm up to 15 μm (Fig. 14d).

It has been found that a flagellin monomer, prepared from the *Salmonella typhimurium*, consists of four linearly linked domains: D0, D1, D2 and D3. Comparative analysis of the flagellin amino acid sequence from different bacterial species revealed that secondary structure of the D0 and D1 domains is mainly the alpha helix, while the D2 and D3 domains are mainly beta sheets. During polymerization, the D0 domain of the monomer the closest domain to the filament axis and the D3 domain is farthest from it (Fig. 14a, Fig. 14c). Analyzes of the polymerization properties of flagellin has shown that during the formation of the filamentous structure, the molecule undergoes a large conformational rearrangement.

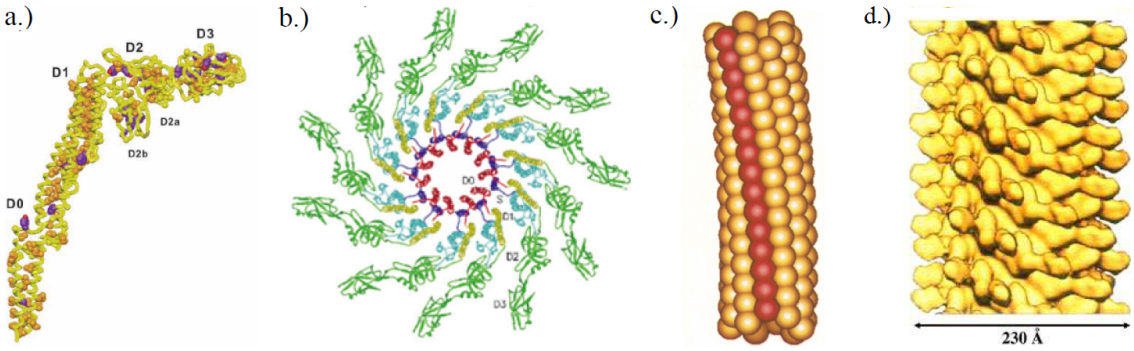

Figure 14: a.) The four domains of a flagellin monomer (D0, D1, D2 and D3) b.) The concentric organization of flagellin subunits c.) Protofilamentally structured so that the D0 domains are inward, the D3 domains look outward d.) Multiple concentric levels constitutes the 23 *nm* diameter filament [32].

Studies have shown that the D3 domain can be removed, modified or replaced by foreign proteins [33]. For example xylanase enzyme can be implanted by using the appropriate linking segments in place of the D3 domain (Fig. 15). The flagellin-xylanase fusion protein was able to form filaments under suitable conditions showing xylan-degrading catalytic activity [34]. Similarly, fusion with other enzymes may also be prepared. Nanostructures capable of controlling coupled reactions with up to thousands of catalytic units from polymerisation-capable enzymes can be constructed this way.

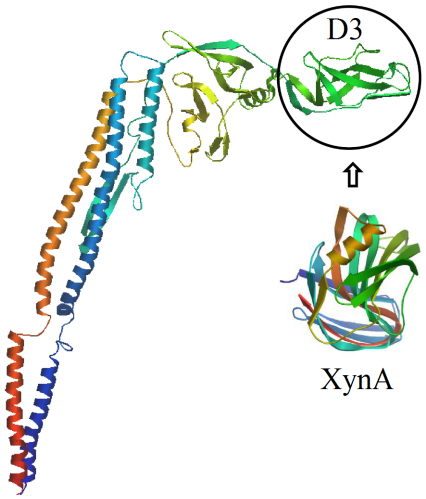

Figure 15: The hypervariable D3 domain of *Salmonella* flagellin (residues 190–284) was replaced by xylanase [34].

On the other hand, the surface of the D3 domain extending from the filament is constituted by three loop regions. By modifying the amino acid sequences of these we can form specific binding sites on the monomer that are easily accessed by the binding ligand. That is why the target of our flagellar filament based biosensor research is based on the D3 domain and its specific genetically engineered modification. The D3 domain can be modified by genetic engineering such, that the FFs do not lose their ability to polymerize and the filamentous structure is not modified through intervention. Since a flagellar filament can be composed of tens of thousands of flagellins, a highly sensitive FF-covered sensor surface can be created.

Fgn is a good reference protein to study flagellar filament isolates, because it is smaller protein than FF, so making an optical model for it was simpler. With that knowledge, we could move on to the filaments.

2.6.2 Production of flagellar filaments

As mentioned above, *in vivo* polymerization process is self-organizing and spontaneous. During its polymerization, the monomers migrate through the filament internal channel to the end of the filament initiation, whereby the HAP2 helps to integrate them. The binding always starts from the C-terminal of the flagellin subunit it binds to the N-terminus of the last monomer of the filament. To get the final form, a few tens of thousands of monomers are required for the polymerization of filament.

However, spontaneous filament formation does not start *in vitro*, because the filamentous domains D0 and D1 have a disordered structure, and thus the monomers are not able to bind together. Therefore, filament initiations or a precipitating agent (for example: ammonium sulfate) are required for the polymerization of flagellin. Usually $0.6-0.8$ M of ammonium sulfate is added to the discrete monomer solution. After rapid mixing, a homogeneous reaction mixture is formed and the polymerization happens quickly.

Polymerization can be influenced by many factors such as: flagellin, physiological conditions (temperature, ionic strength, pH). For the production of a flagellin monomer solution for *in vitro* polymerization, a bacterial colony is generally grown at ~ 37 °C in a culture medium. After the appropriate quantity has been reached, filaments are separated from the other elements that build the cell by long-lasting purification steps.

The monomerization of filaments is achieved by heat treatment at 70 °C for 10 minutes. The true monomer solution is precipitated by a ammonium sulfate and after that is polymerized. This process is followed by buffering to remove the residual agent. After centrifugation, only pure filaments remain in precipitate form. Till the start of the measurement, they should be stored in a refrigerator at ~ 4 °C. For our measurements, flagellar filaments of wild type *Salmonella typhimurium* SJW1103 are provided by the research team of the Technical Chemistry Research Institute at Pannon University.

2.6.3 Qualification of flagellar filament based sensors

An important criterion for the production of reliable, useful bio-sensors is to create a thin layer of high-quality recognition elements in a controlled manner. Therefore, a unique plating of an unknown layer on the transducer's sensor surface can be qualified for qualitative measurements only, it is not suitable for calibrations nor measurements. That is the reason why, it is so important to develop a method by which we can state an objective view of the result of the immobilization of the protein layer on the sensor surface.

As mentioned above, the outer region of the flagellin subunits that form the flagellar filaments can be modified without damaging the filamentary structure. By artificially altering this regions, filaments can be made suitable for specific target molecules, so they can be used for sensory purposes. As each of them is composed of tens of thousands of flagellin subunits, an extraordinary surface recognition density can be achieved, such that the layer of flagellar filaments is not two-dimensional, but in the test solution will be a densely packed three-dimensional system with hundreds of nanometers of filaments. This is a huge advantage over many two-dimensional layers, which makes them suitable for use in a good sensory layer.

As it was discussed in the section 2.6.2, the FFs' advantage is that they can be quickly and cost-effectively produced by bacteria. Separation does not require complicated purification and filtration processes which, for example, characterize the production of antibody recognition elements. On the other hand, they have extremely attractive properties e.g. they are chemically very stable. Since bacteria have a huge development history, they have been able to withstand the harsh conditions over time.

The measurement method plays a major role in the preparation of the sensors. SE is highly suitable for high-sensitivity and non-destructive grading of the complex structures of FFs. The *in situ* measurements in flow cell (Ch. 4) can be used to determine changes in the bulk density of the building layer on the surface. Of course to establish this change a proper model is required. In addition, the depth distribution of the parameters can be measured by perfecting the model. An estimation can be made of the three-dimensional structure of the flagellar filament thin films. These will be discussed in section 6.1.1. By using this estimation, it is possible to further improve the performance of the biosensor.

3 Objectives

My aim was to assist the development of a flagellar filament based biosensor. Accordingly, the main consideration was to better understand the adsorption of the filaments and to get the density-depth profile of the protein layers.

Since the flagellin monomers are considered to be sufficiently large proteins, it is necessary to initially examine a smaller already mapped ones. Thus, initially, I focused on understanding the fibrinogen's adsorption and emerging structure.

Therefore, *in situ* flow cell measurements were required. Since we use a new kind of measuring set-up, a new, well usable, but still simple, model was needed. Based on the above, I sought to do this.

To validate the measurement and analysis results and to understand the microscopic homogeneity of the emerging structure, additional alternative measurements were required. For these purposes we mainly used AFM. Also by doing so, the aim was to get the length distribution of the proteins used.

To even better understand the emerging kinetics and layer structures creation of a simulation was necessary. Making another program was also my goal, that will be able to find the best simulation result that is appropriate to the given measurement and best describes it. I would like to use the correlations from these to further understand the adsorption of fibrinogens and filaments.

4 Experimental methods

4.1 Plasmon-enhanced two-channel *in situ* Kretschmann bioellipsometry

Because of not only the initial nor the final states of an adsorption process can provide information, but also its kinetics, therefore it is useful to observe the adsorption *in situ*. This is why flow cells are developed for specific bioellipsometry measurements. In most of the cells the solid-liquid interface is measured through the liquid at a certain angle of incidence (AOI) (Fig. 16) [35]. Another limitation factor is the the restricted wavelength range due to the absorption of the water.

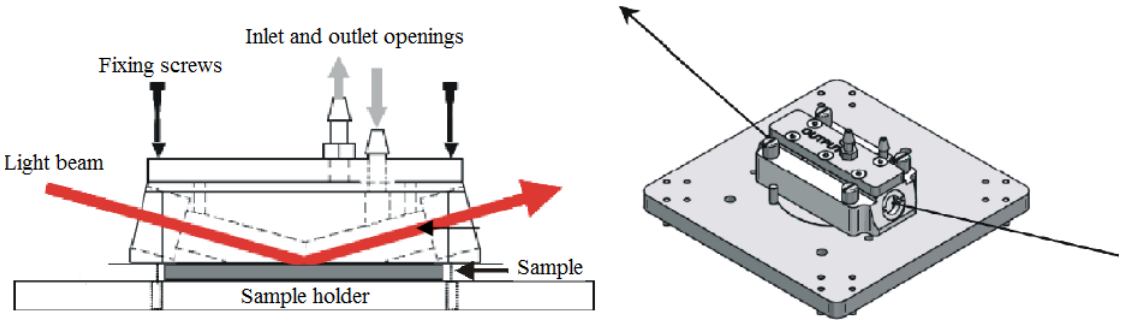

Figure 16: The schematic image of the flow-cell [36].

Our team developed a new flow cell using an internal reflection Kretschmann configuration [37, 38], in which the substrate is positioned upside-down and a semi-cylindrical glass lens is placed above it (Fig. 17). The interface is measured from the substrate [39] through a plasmonic gold layer [40] and we can do dual-channel measurements with it. The gold layer on the samples was created by e-beam evaporation. To enhance the adhesion of gold film to the glass 2 nm Cr_2O_3 layer was added. The glass slide is attached to the bottom part of the semi-cylinder, between these there is an immersion oil (*Zeiss* Immersion OilTM 518) layer to avoid the formation of an air gap (the refractive index of the oil and the BK7 glass is the same).

At this configuration any AOI can be chosen between 45° and 75°. Due to the configuration the light beam is always perpendicular to the window. For each sample we use different angle of incidence where the plasmon resonance is the highest to maximize the effect and so the sensitivity of the measurement. Also this

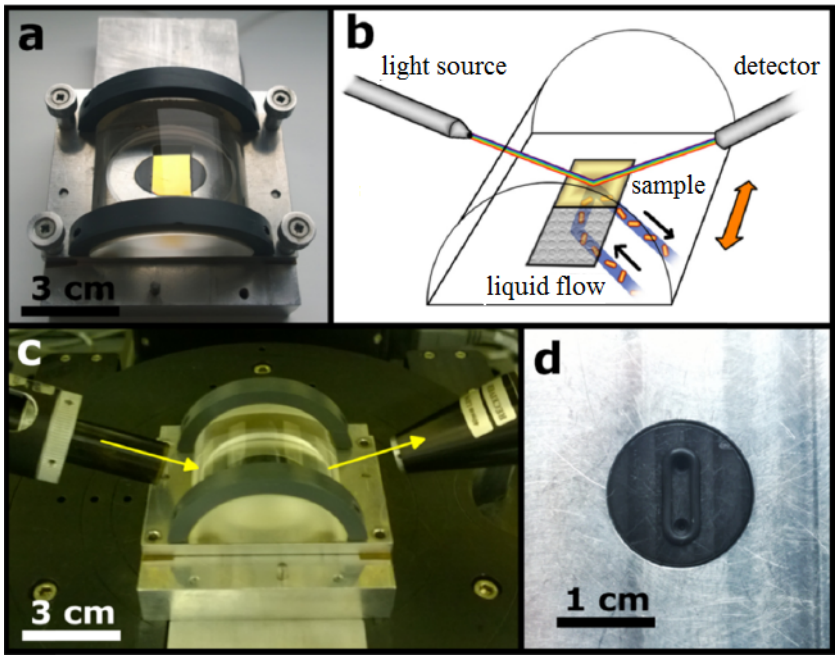

Figure 17: a.) A photo of the assembled glass semicylinder with the gold substrate. b.) A schematic image. c.) Photo of the measurement geometry. d.) The 10-μl flow cell is surrounded by an O-ring [17].

configuration can utilize a larger range of wavelengths. Another main feature of the new flow cell that this construction is less sensitive to bubbles, also due to the small volume of the cell (10 μl) since only little time needed to replace the ambient inside the cell. In our two-channel version of the new configuration simultaneous *in situ* measurements can be made in two differently prepared surfaces in the same liquid cell within the same measurement. The advantage of the method is the multi-channel capabilities of advanced biosensing techniques. The best limit of detection is achieved when using a gold layer with a thickness of 40 nm, and angle of incidence of 70°, and a wavelength of 770 nm [41].

The the flow cell is placed on the stage of the ellipsometer and we use lenses to focus the light of the ellipsometer on the solid-liquid interface at the bottom of the semi-cylinder (Fig. 17b). The variation in the angle of incidence caused by the glass is below 0.5°. At the end the light beam is projected on the substrate as a small spot (0.3 mm $\times$ 0.9 mm). At specific settings the whole spectrum can be measured less than 1 s. The liquid with the dissolved protein molecules can be flowed continuously, so that we can measure the process of protein adsorption in real-time by this method.

4.2 Preparation

Before the measurements are started, the instrument and flow cell must be calibrated. The instrumental part can be acquired quite simple by measuring the known thickness of a thermal oxide Si layer of a single Si wafer. On the other hand it is not as simple and even complex if you are working with a flow cell. When the ellipsometer is switched on, the stepping and servomotors are set to zero by the controlling *CompleteEASE* program. The calibration of the polarizer and the analyzer is also possible using the software and a reference sample. But these settings are rarely modified, for example, when initializing the instrument for the first time.

In order to maximize the intensity of the light coming into the detector, the optimum height and tilt of the sample holder must be set. The instrument can do this automatically, but in case of samples with large dispersions or samples that are not perfectly flat we skip the automatic alignment process and manually adjust the setting. The surface of the detector is divided into four segments. Depending on the amount of light intensity each segment gets, it controls the pitch of the holder. The height is adjusted using a top-mounted red laser. Mostly we use the manual setting to measure in the liquid cell.

The adsorption measurements were carried out on substrates consisting of three layers: a glass, a Cr_2O_3 layer with thickness of 2 nm and at the top a 40-nm Au layer. As I mentioned earlier, the cover glass was coated by e-beam evaporation of Cr_2O_3 and gold thin film. It was purchased from the *Optilab Ltd., Hungary*.

The samples and each part of the measuring cell, in particular the metering volume, are alternately cleaned by ultrapure milli-Q water (MQ) and methanol (VWR Chemicals), each step lasted for $\sim$ 10 s. Also the substrates and the flow cell are dried with nitrogen gas between and after the cleaning steps. This cleaning process is always done to all samples. It is a necessary step, because different surface impurities can remain on the flow cell's surface and the other reason is that hydrocarbons are adsorbed to the gold surface from the air and they have to be removed. In summary, the cleaning procedure increases the reproducibility of the measurements. If the process is performed correctly we get surfaces with the same characteristics.

4.3 Protein adsorption measurements

During protein isolation, we strive to make them under similar experimental conditions. During my measurements and during the measurements I used, we also followed this principle. Of course, there are many other experimental groups, so sometimes we put emphasis on other parameters, so there are measurements where we have deviated from normal steps.

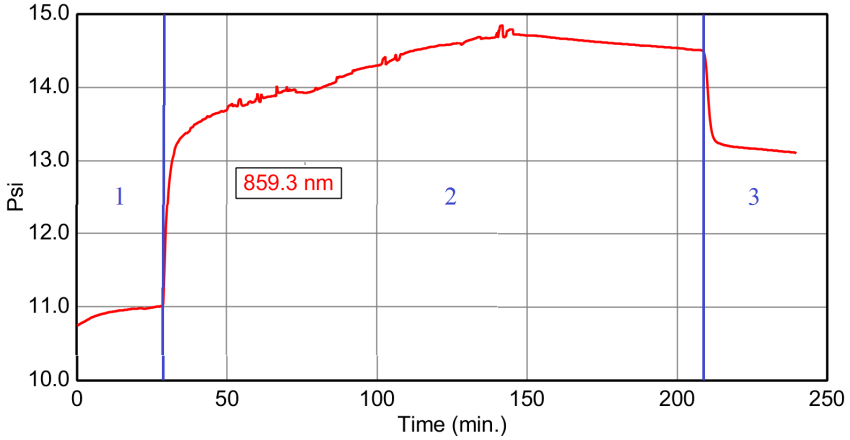

Figure 18: Ψ dynamic data of flagellar adsorption at 859.3 nm. Three distinguishable parts of measurement: PBS baseline (1), protein adsorption phase (2) and washing with PBS (3).

The curve shown in Fig. 18 depicts a typical protein adsorption process. The resulting curve serves as detailed depictions of the phases of the layer formation process as shown by the adsorption of flagellin. Due to smaller size of fibrinogen, it causes minor changes in Ψ, so the phases would be less isolated.

During the experiments we used protein solution with different concentrations. The 20 mM phosphate-buffered saline (PBS) solution was reconstituted by MQ water and water-soluble tablets. Protein adsorption was *in situ* investigated during fluid flow. Continuous flow in the liquid cell was provided by a peristaltic pump. The flow cell has an inlet or outlet tube, and a rubber guard, which allows precise and airtight surface fixing.

First, the cleaned sample's SE spectrum had been recorded. The evaluation of the spectrum results in fitting parameters (thicknesses, refractive index) that were recorded for a further phase of the measurement. The cell was fixed with screws on a metal plate on which the sample lays. The next step was to measure the spectrum at different angles and select the angle at which the highest sensitivity was observed.

The ellipsometer recorded a spectrum from the surface per every 6 seconds in two channels to precisely monitor and follow the changes in the surface. The data capture time can be varied, so it is advisable to increase this for longer (multi-hour) measurements for easier data processing. We can distinguish three different parts in Fig. 18. In the 1st and 3rd steps, a buffer flows through the liquid cell over the sample. The flow rate can be adjusted, it does not significantly change the maximum amount of adsorbed material, but by increasing the flow rate the saturation (smaller time constants) kinetics change. During the measurements the flow rate was ~ 1 $\mu l/sec$. From the point of view of evaluation, the buffer sections are extremely practical, as in the corresponding optical model, the environment, PBS, is always the same. So it is enough to concentrate on the other variable components.

The baseline was recorded until the measured ellipsometric angles (such as media parameters) stabilized and then changed to a protein solution (2nd step). At this stage, the given concentration of the protein passed through the cell, we use a big variety of concentration from 0.005 mg/ml up to 0.5 mg/ml. The initial phase is extremely fast, so this part is the object of our study.

Because the measurement is not only *in situ*, but also real-time (i.e., measured data and model used are already available during measurement), so after reaching saturation we could start PBS washing (3rd step). Proteins that had not been bound to the surface and were just stuck on the fixed proteins can be removed during PBS washing. Thus, during the evaluation, the amount of material actually adsorbed can be determined.

For the pairs that differed only in one experimental parameter, we tried to reconstruct the duration of each phase as accurately as possible. Based on *Castro*'s results [42], only 3 parameters from the tested ones significantly affect protein adsorption: the temperature used to store the protein, the temperature difference between the cell and the solutions and the degree of hydrolysis of the substrate. Thus, for example, cell purification does not significantly affect the results of the measurements, but the purification process has to be done, only the method can be different. Another example is the temperature of the laboratory during the experiment also does not effect the adsorption significantly.

After measurements, the samples were rinsed with milli-Q water and then purged with nitrogen to allow the surfaces to be studied with an AFM. The salt from the PBS buffer can be removed by rapid flushing with MQ water.

4.4 Modeling of adsorbed fibrinogen layers

The above-described thin layer system can not be considered with a single optical model. However, which one is the most suitable evaluation method, we can decide by comparing the error values of the parameters calculated and the matching mean value of the mean squared error. From the foregoing, we can conclude the

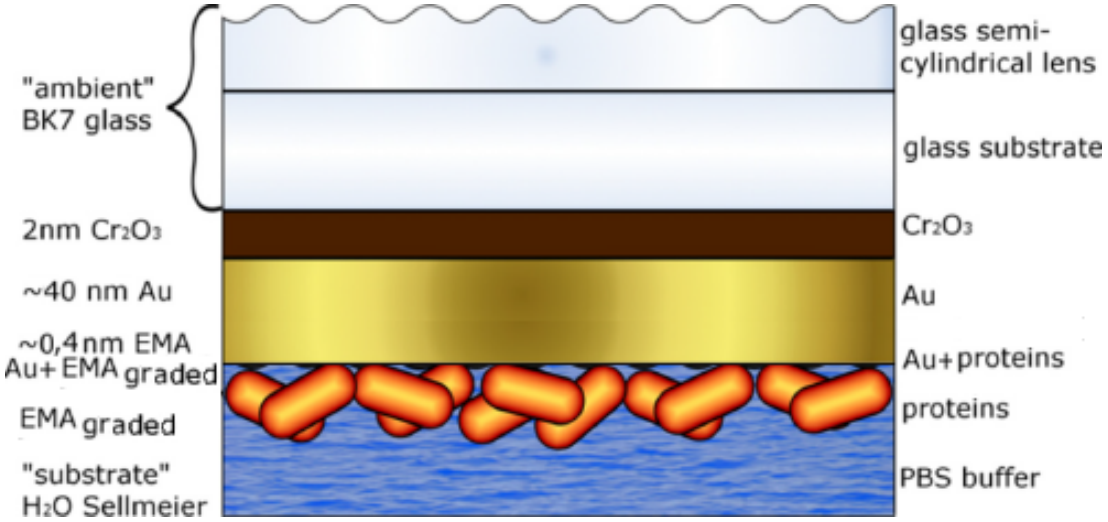

Figure 19: The physical layers in the protein adsorption measurement (on the right) and the corresponding layers of the ellipsometric model (on the left) [17].

correlation between the parameters. The MSE characterize the goodness of modeling on the measured Δ and Ψ spectra.

I compared many different models, the following one describes the layers the best (Fig. 19). Due to the Kretschmann configuration, the ambient was set to BK7 glass (Cauchy), the refractive index of the oil between the gilt glass and the glass cylinder matched, so I regarded this whole system as one. The parameters of this Cauchy materials are: $A = 1.471$, $B = 0.015$ and $C = 0$. The optical model consists of a stack of 2 nm Cr_2O_3, $\sim$ 40 nm gold, protein layer and the PBS as a substrate. The gold layer's thickness was always fitted and its roughness as well by an EMA of Au and graded EMA of proteins and PBS (substrate) as shown in Fig. 19. The PBS medium was taken into consideration also with the Cauchy formula and the fibrinogen layer with the graded EMA model.

For PBS buffer, I have fitted the parameters of the Cauchy model in the case with no proteins. Thus, at 632.8 nm, the refractive index of PBS was $n = 1.3261$. The refractive index can be accurately determined to the fourth decimal place. The

protein filled EMA model is a combination of the already known refractive index of the buffer and another Cauchy refractive index dispersion, where the parameters of the protein are: $A = 1.45$, $B = 0.01$ and $C = 0$ were fixed. The refractive index of the protein corresponds to the range of $1.3 - 1.5$ according to the literature [10].

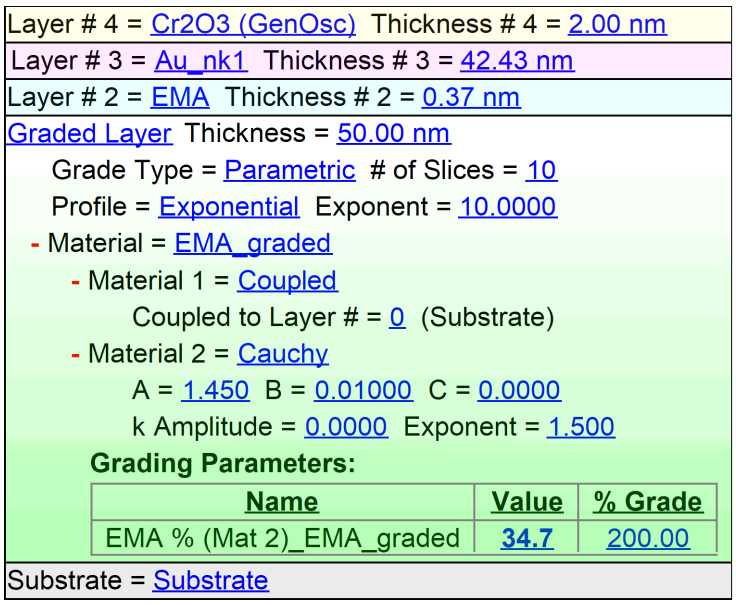

Figure 20: The optical model that describes the flow cell in the presence of fibrinogen protein layer.

The protein buffer EMA is a non-trivial optical layer (Fig. 20). For fibrinogen, the thickness was set to 50 nm, this fixed thickness value describes the measurement the best. The layer can be divided into an optional amount of sublayers, in which case I have always chosen 10 sublayers. The software calculates the ratio of proteins and PBS to each sublayer and then averages it. As getting away from the surface, proteins take less and less volume percent of the sublayers. On the other hand, due to the exponential decline of the evolutionary wave, by moving away from the surface the measurement becomes more and more insensitive. So I compared the relationship between the sub-levels with an exponential function. The corresponding exponent was 10 in case of the fibrinogen.

Every time I fitted the protein percentage *in situ* in the layer, in each case the MSE was below 17, which is still acceptable. This value shows that the model is approaching the measurement, but even better and more accurate one can be created. Based on this fibrinogen model, I have prepared my other models of flagellar filaments.

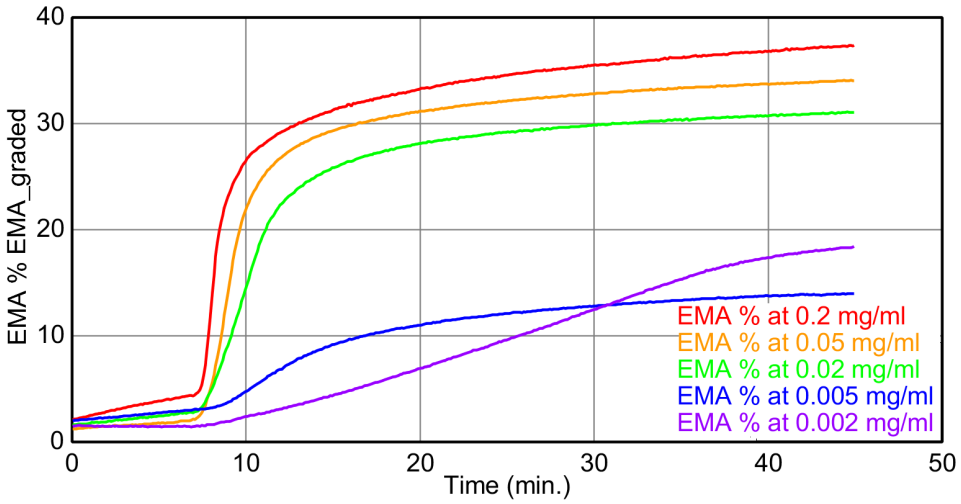

Figure 21: The kinetics and the EMA values of fibrinogen at different concentrations.

4.5 Modeling of adsorbed flagellar filament layers

For flagellar filaments, it is more difficult to create an optical model than the adsorbed fibrinogen layer, since the size of the FFs is much larger and more elongated. Their length typically varies in the range of $300 - 1500$ nm, which makes the evaluation more complex. I tried the multi-layered EMA-approximation of adsorbed FF, but the results did not give the best match between the calculated and measured spectra of the model.

Layer # 4 = Cr2O3 (GenOsc) Thickness # 4 = 2.00 nm
Layer # 3 = Au_nk1 Thickness # 3 = 42.64 nm
Layer # 2 = EMA Thickness # 2 = 0.47 nm
Graded Layer Thickness = 500.00 nm
Grade Type = Parametric # of Slices = 10
Profile = Exponential Exponent = 3.5000
- Material = EMA_graded
- Material 1 = Coupled
Coupled to Layer # = 0 (Substrate)
- Material 2 = Cauchy
A = 1.450 B = 0.01000 C = 0.0000
k Amplitude = 0.0000 Exponent = 1.500
Grading Parameters:

Name	Value	% Grade
EMA % (Mat 2)_EMA_graded	1.0	200.00

Substrate = Substrate

Figure 22: The optical model that describes the flow cell in the presence of FF protein layer.

Then I used the same EMA model I used for fibrinogen, with little changes in it (Fig. 22). The parameters of the Cauchy model for the protein were again fixed: $A = 1.45$, $B = 0.01$ and $C = 0$. In this case, I also divide the layer into ten sub-layers. The best results were achieved by the 3.5 value of the exponent. In the model, the variable parameter was the protein volume. Estimated layer thicknesses d were recorded in the EMA model and within the thickness layer I determined the volume percent of protein by fitting. I also fitted the measured spectra with different thicknesses and several EMA layers, and I came to the conclusion that at $d \sim 500$ nm the MSE was the smallest. On the basis of the evaluation, close to the surface (~ 50 nm) the percentage of protein was 1.61%, further from it (~ 200 nm) the volume was 0.43%, in this case, the concentration of protein solution was 0.02 mg/ml. This means a larger amount of adsorbed material near the surface.

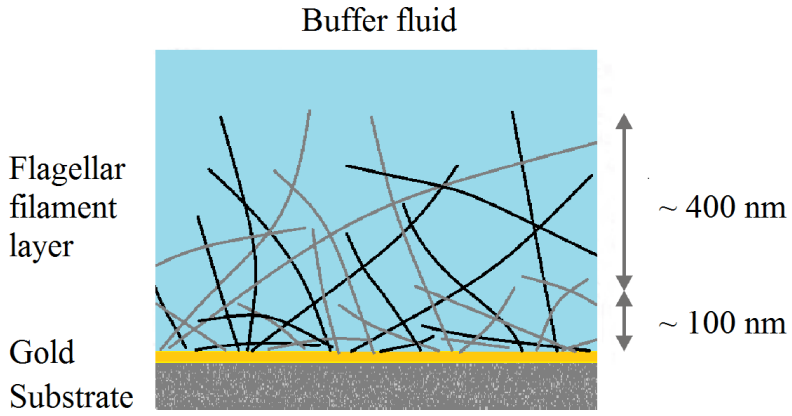

Figure 23: Schematic diagram of the adsorbed FF layer in PBS media.

Thus, on the basis of the model, we expect the filaments to fall or at least not to be perpendicular to the surface, possibly by fixing at some points. But there are proteins with their endpoints attached to the surface, so that their presence can be detected at the distance of ~ 500 nm from the surface (Fig. 23). This complies with the random sequential adsorption (RSA) model for the particles to reach the carrier in random positions, the model will be discussed in detail in section 5.1.2.

Since the protein isolation was measured *in situ*, I could determine the parameters of the EMA layer (volumetric percentages) in time by fitting on all the registered spectra. The filament protein layer was taken into consideration by several EMA models. If the structure was divided into many EMA layers or any gradation in only one EMA, the result was always a denser structure (near the surface) and a lesser part (beyond the surface).

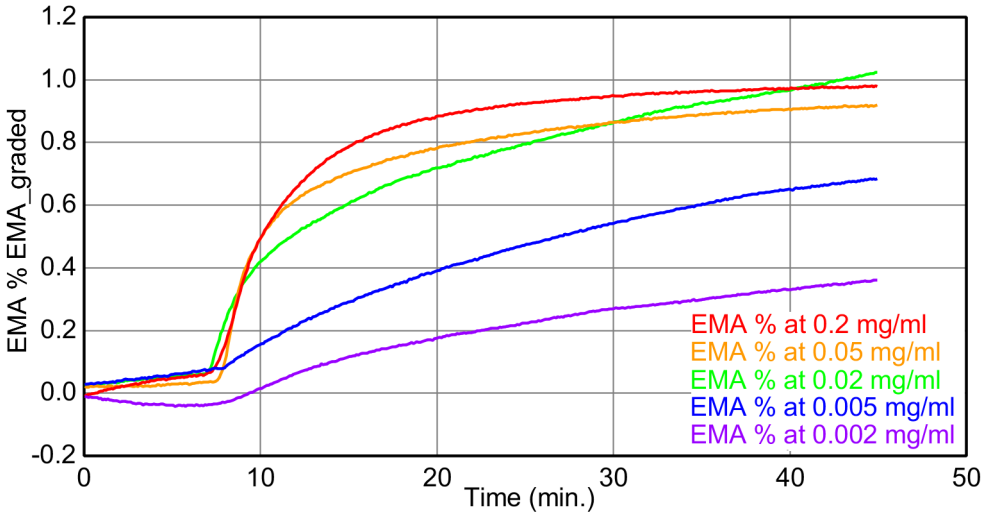

Figure 24: The kinetics and the EMA values of FF at different concentrations.

4.6 *Ex situ* surface analysis

To develop a great FF-based biological sensor it is crucial to know the homogeneity and mass density on the surface after immobilization. Several measuring techniques can be used to answer this questions such as spectroscopic ellipsometry, atomic force microscopy and scanning electron microscopy (SEM). In the cases of SEM and AFM, the difficulties are the image processing, and also the fact that the determination of the quantity of material for quantitative macroscopic surface size is problematic based on these micro-images (a few μm^2). The other main disadvantage that these procedures are highly time-consuming, and that the preparation for *ex situ* measurement and of course the measurement itself damages the samples. That is why, these techniques are not suitable for routine provision of the above-mentioned tasks.

AFM and SEM also have advantages over the SE. We usually use them to check the length distribution of the adsorbed FFs. We cannot get this information from ellipsometry measurements. The length distribution was examined by using *ex situ* AFM which type was AIST-NT SmartSPM^{TM} 1000. We used AFM tips with 10 nm curvature diameter. By evaluating the AFM images the mean length of the adsorbed flagellar filaments was able to be determined, and systematically compared with the results of SE investigations. By applying lower protein concentrations or lower deposition time, lower surface coverage can be obtained on the surfaces (Fig. 25). Also, we use them to support and validate our results. In addition, we look

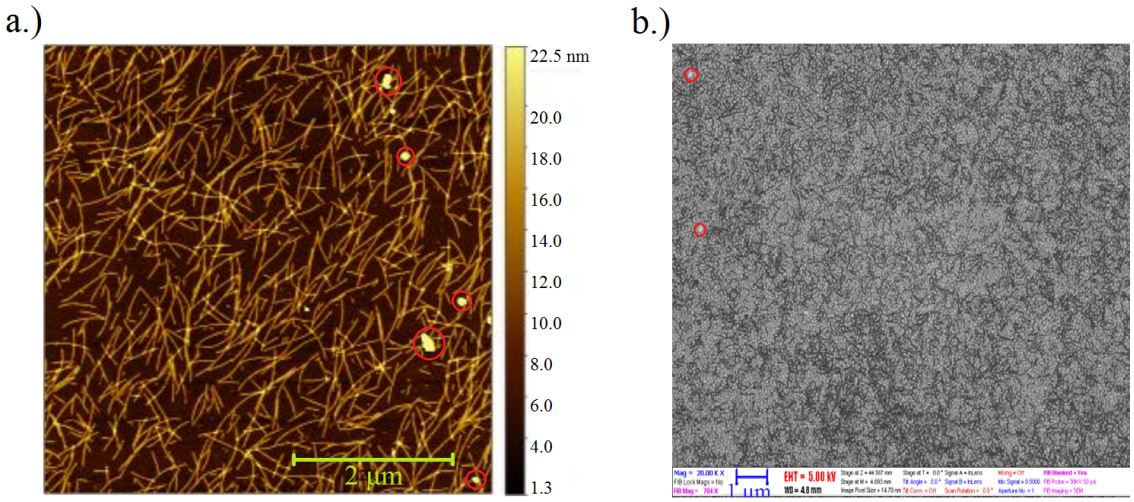

Figure 25: Pictures of gold surfaces covered by flagellar filaments made by a.) AFM and b.) SEM (AFM images were taken by me, Benjamin Kalas and Jutka Nádor and SEM by Levente Illés).

at the actual surface structure, local envelope, and possibly emerging patterns, the causes of cracking. In case of SEM, information about the formation of salts or impurities (areas marked with red circles in Fig. 25) can also be obtained.

As I mentioned in the previous paragraph, the length distribution of the FFs can be determined by AFM and SEM. The measurements were performed under previously mentioned conditions. Before the procedures, the samples were taken out of the cell, they were rinsed with MQ, were discharged with nitrogen and were stored in a sample holder. It appears in Fig. 25a that on the dried surface, the protein fibers are dull and therefore overlap in many places. The orientation of the filaments can be the result of flow rate or washing and nitrogen purge. Image processing program allows the AFM images to be used to determine the length distribution of filaments.

The result showed a significantly shorter value and a significantly higher dispersion length: $l \sim 500$ nm and $\sigma \sim 200$ nm, than expected on the basis of ellipsometric measurements: $l \sim 600$ nm and $\sigma \sim 30$ nm. The difference can be justified by a number of reasons, we should not forget the factors influencing the result: the treatments before AFM and SEM measuring involves the fragmentation, depolymerisation, or partial (possibly size dependent) leaching of the bounded flagellar filaments. Also, overlapping filaments make it difficult to process the images.

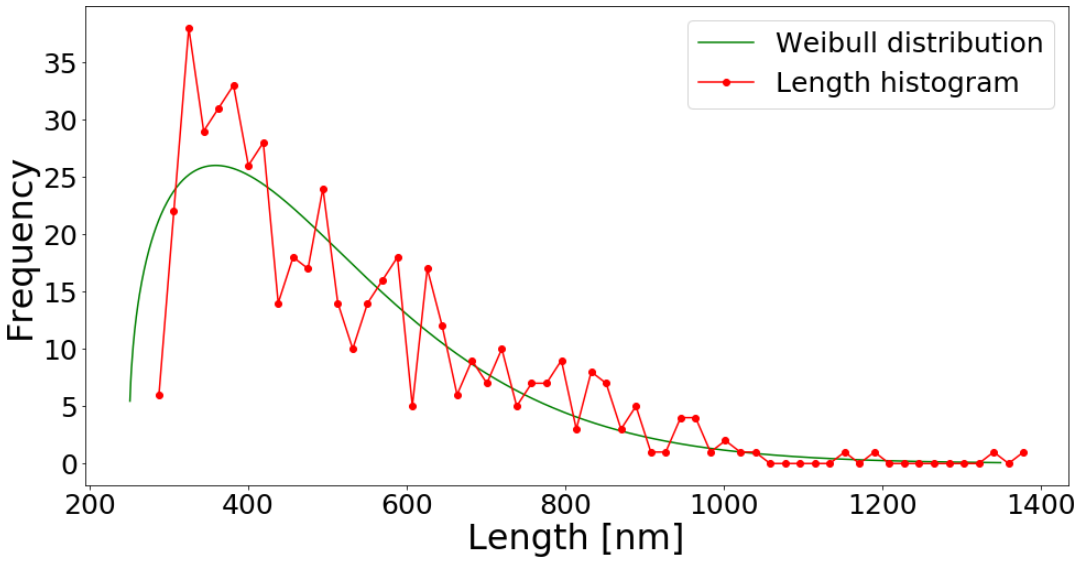

Figure 26: The length histogram and the fitted Weibull distribution.

The obtained length distribution can be described by the Weibull distribution (Fig. 26). Its density function can be given by the following equation:

$$f(l, L, \mu) = \begin{cases} A\frac{\mu}{l}\left(\frac{l}{L}\right)^{\mu} e^{-(l/L)^{\mu}} & l \geq 0, \\ 0 & l < 0, \end{cases} \tag{40}$$

where A is the amplitude, L is the average size of the particles, μ is the shape parameter and l are the different length values.

On the other hand, using optical measurement techniques, the quality of the FF layers can be achieved quickly, easily, routinely, in large quantities, even when immobilized on the sensor surface. SE is a high sensitivity method that provides global information on the thin layer structural parameters in a wide wavelength range: thickness, density and even lateral homogeneity. Using this method can be the key to the development of the reliable production of new sensors.

5 Protein adsorption

5.1 Protein adsorption models

To describe the adsorption of proteins on the surfaces, we need to have the physical and chemical background of the processes. Generally, the proteins are not strongly bound to the surface (which requires a chemically activated surface), but they are bound by *van der Waals* or ionic interactions. In order to understand and simulate the processes, we often have to use approximations. In this and in the next sections I will discuss the most commonly used and proven descriptions.

For simplicity, we assume that our particles are spherical, smooth and rigid, and we turn off the gravity. Far away from the surface, the flow is not affected by the surface, as opposed near the interface, due to friction, the speed of the liquid (parabolic flow) is reduced. A particle of the solution can reach the surface through the flow of the solution (convection) and diffusion [43]. Therefore, the particle moves near the surface with diffusion and far away from it by flow. Within a certain distance, the particle flow-driven transport is transformed into a diffusion motion, this is the diffusion boundary distance - d (the order of magnitude of the d is some ten micrometers, taking into account that the geometry of the flow is tubular) [44]:

$$d = \left(\frac{3}{2}\right)^{\frac{2}{3}} \left(\frac{DC}{\nu}\right)^{\frac{1}{3}}, \tag{41}$$

where D is the diffusion constant of the protein, ν is the flow rate, and C is a constant, which is dependent on the geometry of the flow pipe (volume dimensional).

Adsorption requires new and new particles to flow to the diffusion interface. In order for these proteins to stick to it, another control factor should be taken into consideration, the surface envelope. Taking into account the above, the protein adsorption kinetics can be described by the following general context:

$$\frac{d\Gamma}{dt} = k_a c\, \phi(\Gamma) - \Gamma\, k_d\,, \tag{42}$$

where Γ is the known surface adsorbed mass density (μg/cm^2), $\phi(\Gamma)$ is the available surface function (ASF), and k_a and k_d are the adsorption and desorption rate constants respectively (cm/s), and c is the concentration of protein solution (mg/ml).

$\phi(\Gamma)$ has an important role in the description of kinetics. In the case of $\phi = 1$, there is no adsorbed protein on the surface, so the entire surface is free to be available for the particles. The function ϕ can be determined by series expansion and parameter matching:

$$\phi = 1 - C_1\Theta + C_2\Theta^2 + \dots, \tag{43}$$

where Θ is the surface covered by adsorbed particles. C_1 corresponds to the surface area blocked by a single particle, whereas C_2 denotes a cross-section of the area blocked by two independent molecules. The C_i parameters may be different for different models, which can be determined by simulation.

5.1.1 Langmuir model

One of the most used adsorption models is the Langmuir approximation. The model explains adsorption by assuming an adsorbate behaves as an ideal gas at isothermal conditions. It is assumed that the surface is composed of separate active bonds (Fig. 27). The adsorption of the particles is not affected by adjacent active site-bound molecules (overlapping excluded) and the layer does not exceed the monolayer structure ($\Gamma_{monolayer}$ is the total amount of material in monolayer).

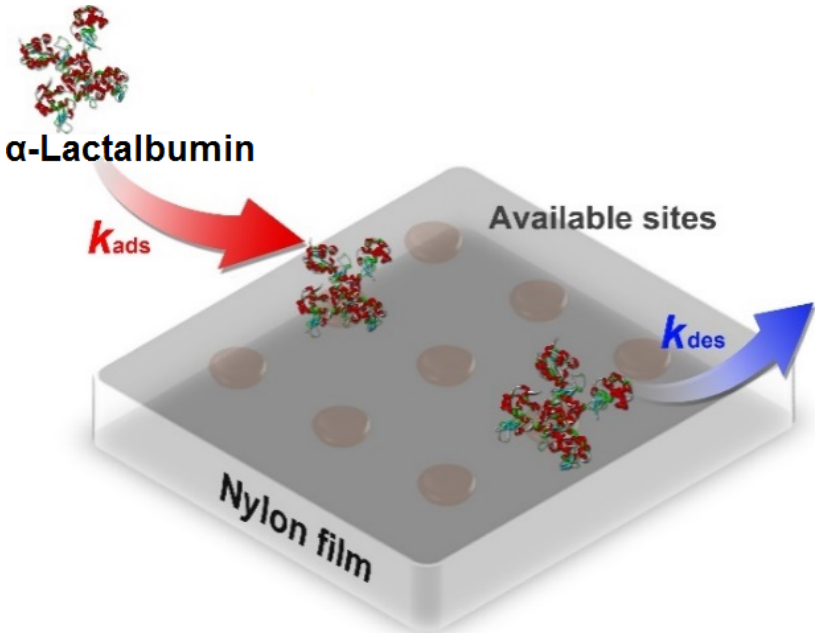

Figure 27: The adsorption of a α-lactalbumin on chemically identical but morphologically heterogeneous polymer surfaces [45].

The approximation permits particle desorption from the surface, the kinetic equation thus takes the following form:

$$\frac{d\Gamma}{dt} = k_a c \left[1 - \frac{\Gamma}{\Gamma_{monolayer}}\right] - \Gamma\, k_d\,. \tag{44}$$

The solution of the equation can be approached with an exponential function. The C_i parameters in case of the Langmuir model are $C_1 = 1$, $C_2 = 0$ and $C_3 = 0$.

5.1.2 Random sequential adsorption

Random sequential adsorption refers to a process where rounded particles are randomly distributed in a system, they reach the surface in a random position, and if they do not overlap any previously adsorbed particle, they adsorb and remain fixed for the rest of the process (they irreversibly bind to the surface without lateral displacement, thus excluding the desorption of the particles) [46, 47]. The shape of the particles can be spherical, cylindrical, elliptical and rectangular. Since the particles randomly reach the surface without overlapping, the relation $\phi < 1$ generally exists. With the increase in the amount of adsorbed surface material, the likelihood

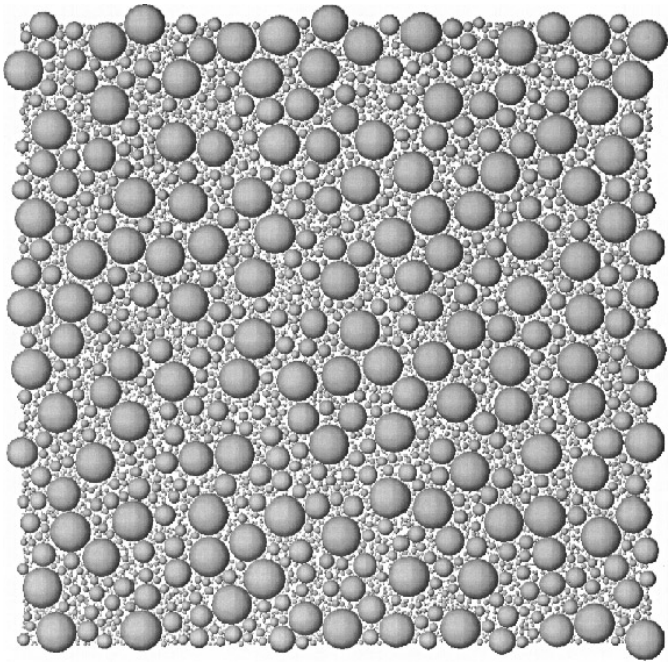

Figure 28: A computer realization of a classical RSA model of deposition onto a plane surface with exclusion of overlap [48].

of adsorption is reduced as the overlap between the particles is excluded. Saturation occurs if the likelihood of adsorption decreases to zero (Fig. 28). In this case, the kinetic equation assumes the following form:

$$\frac{d\Gamma}{dt} = k_a c\, \phi(\Gamma)\,. \tag{45}$$

In the case of very elongated particles, the surface coverage is the following:

$$\Theta_\infty(\alpha) \sim \alpha^{-\frac{1}{1+2\sqrt{2}}}, \tag{46}$$

where α is the ratio of the longitudinal axis and shorter axis of the particle. Knowing the C_i parameters, the kinetics can be obtained, and the differential equation for Γ can be easily solved.

5.2 Comparison of fibrinogen and filament adsorption

As I have already mentioned, fibrinogen is a good model protein to better understand the adsorption of more complex proteins such as flagellar filaments. I compared their kinetics by fitting different functions to the measurements. The further chapter aims at the kinetics and the resulting structure of the FF. Each model (Langmuir and RSA model) predicts linear growth of the material quantity at the beginning. After the linear phase, the Langmuir model predicts a rapid exponential growth (47), while RSA approximates the curve with a slower - algebraic function (48).

On this basis, we distinguish transport limited and adsorption limited regions (Fig. 29) [44, 46]. At the beginning of the adsorption, the particles move by the diffusion towards the surface, so the diffusion speed limits the process. By achieving critical concentration, the number of active free spaces decreases, as adsorption of new particles is continuously ensured. Thus, this region is controlled by a decrease in the number of available sites (adsorption is limited). When the available surface function reaches the minimum, the surface is saturated. In saturation, adsorption and desorption processes are in dynamic equilibrium ($k_a = k_d$).

If we plot $\frac{d\Gamma}{dt}$ as the function of Γ then we have to get linear correlation between them [49], in case there is no transport limitation, the time derivative of the material

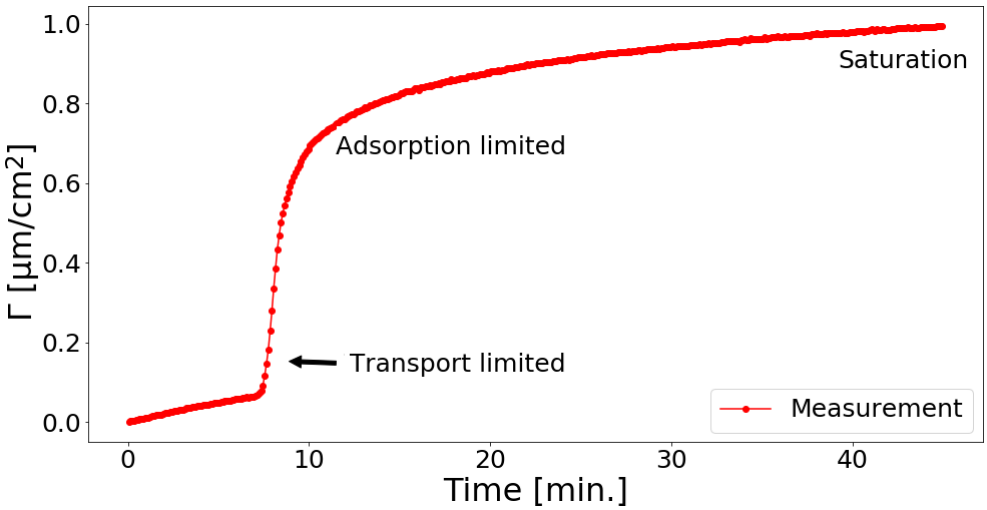

Figure 29: Γ(t) adsorption curve of Fgn at 0.05 mg/ml concentration, indicating the different regions. The protein flow started after 7.5 minutes.

mass density is proportional to the amount of adsorbed mass density (44). If I represent this function for fibrinogen and flagellar filament adsorption, there is an initial transport limited region where the flow and diffusion of the particles control the process. This limitation will cease when new particles are continuously provided near the surface. As the coverage is growing, the surface can no longer bind the molecules fast enough, thus, diffusion will no longer be a limiting factor. So I found that adsorption of FFs and Fgns can be faster than the diffusion. The curve converges to zero, which is the consequence of saturation (Fig. 30).

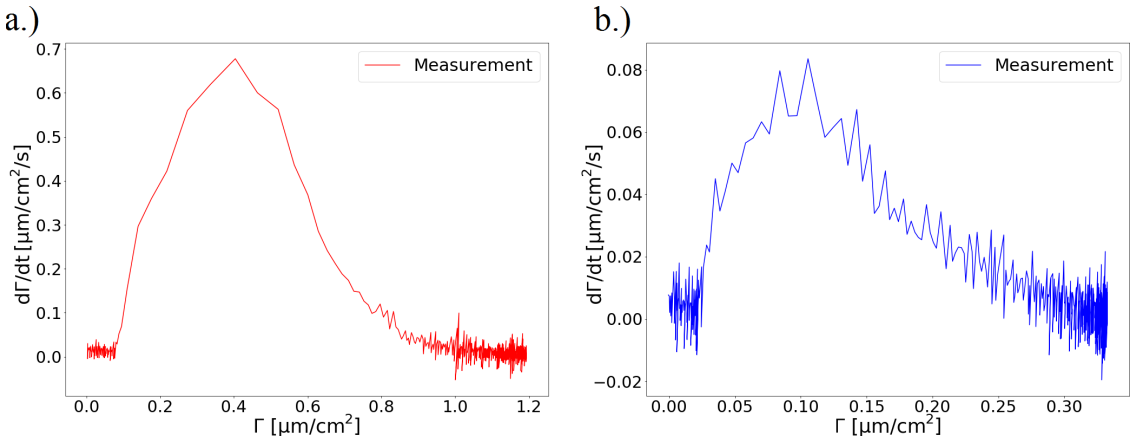

Figure 30: a.) Fgn, b.) FF adsorption at 0.02 mg/ml concentration.

By fitting on the linear parts of the (Fig. 30) (adsorption limiting regions) k_a (cm/s) an initial ($\Gamma = 0$) adsorption velocity constant can be determined. Using the following approximation, that the attachment is irreversible, in this case, the k_d coefficient becomes zero. I have studied many different measurements, for Fgn, the magnitude of k_a is: $\sim 10^{-3}$ cm/s, and for FF they are: $\sim 10^{-4}$ cm/s.

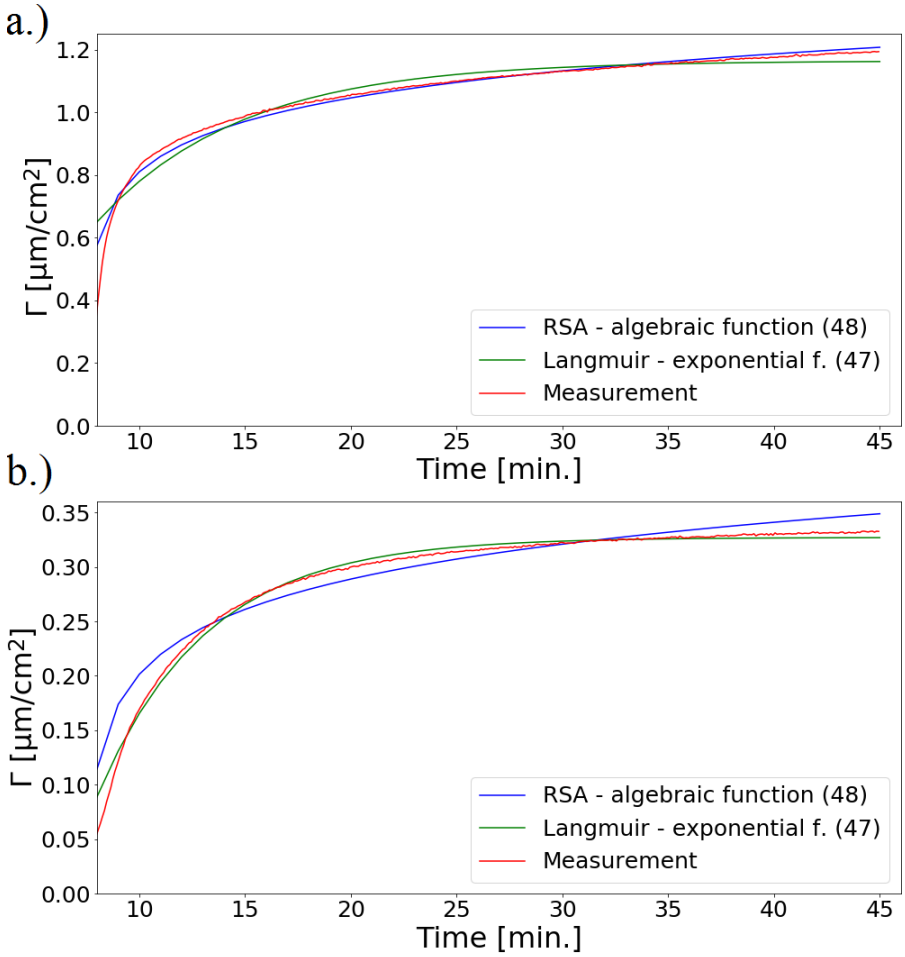

Figure 31: a.) Fgn, b.) FF adsorption curve and the exponential function of the Langmuir model as well as the algebraic functions of the RSA model.

As we have seen above, neither model describes the measurement properly, but they can be used for estimation. I fitted exponential and algebraic functions to the adsorption measurements (Fig. 31), the shapes of which are as follows:

$$\Gamma(t) = A\, e^{-\beta t + c} + \Gamma_0\,, \tag{47}$$

$$\Gamma(t) = A\,(t + t_0)^n + C\,, \tag{48}$$

where A is the amplitude, t is the time, β is the exponential time constant, Γ_0 is the amount of saturation material and n exponent is a parameter dependent on the geometry of the particles. On the basis of the RSA model, saturation is much slower, due to the fact that it takes into account the change in the ASF function. Both adsorption curves were approached from above by Langmuir model and were approached from below by the RSA model. It can be seen that the real measurement is not accurately described, so the RSA model and the Langmuir model can only be used to approximate the adsorption of proteins.

6 Numerical simulations

The driving force of the numerical simulation is to better understand and obtain the density-depth profile of the flagellar filaments in the buffer environment, and to gather more information about the adsorption kinetics. By using the results obtained from this information we can create better optical model and a more accurate alignment of the SE measurements. Understanding the actual orientation of proteins and the adsorption kinetics in the fluid plays an important role in developing a good sensor. That is why we put so much emphasis on this topic.

The simulation is an approximation of reality, as the particles that represent the protein are cylindrical, straight and completely rigid (the FFs we use can be both straight and beveled, the assumption that the FFs can be described as rigid particles is relevant). The adsorption surface (completely straight) does not entirely correspond to the golden layer we use, which has different faults on the surface and is not completely smooth (Fig. 32). In the resulting protein layer, the FFs do not intersect, they can be maximum in contact with each other. I used a rectangle simulation box with periodic boundary conditions in the x and y directions (2 μm $\times$ 2 μm box, from this huge size the deviation in the resulting layers is less than 1%). In $z > 0$ direction the box's size was unlimited.

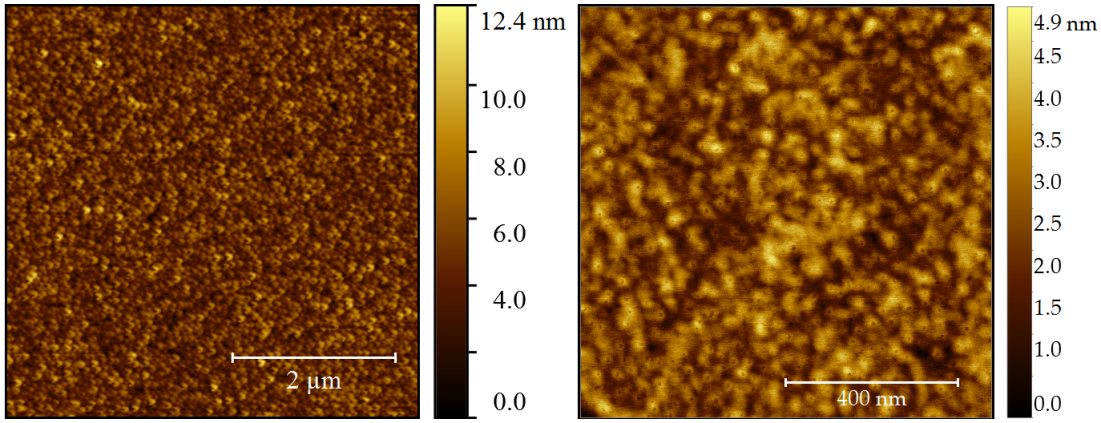

Figure 32: AFM images of a Au coating created by e-beam evaporation on glass substrates (the images were taken by Benjamin Kalas).

During the simulation, more and more particles stick to the surface at their endpoints ($z = 0$ and random generated x, y coordinates). The length of the cylinders was chosen for the different distributions (Weibull, Gauss, uniform) based on the distribution from the AFM measurements. The average length is about

500 nm and the diameter of the FFs is 23 nm, I tried to get the proportions to the best of reality. Each filament has two spherical coordinate angles. While the ϕ (azimuthal angel) describes the angle in the x-y-plane, the θ (polar angle) is the angle out of that plane. In each run ϕ was randomly generated in the range of $0° - 360°$, so the proteins could be in any direction on the surface (Fig. 33).

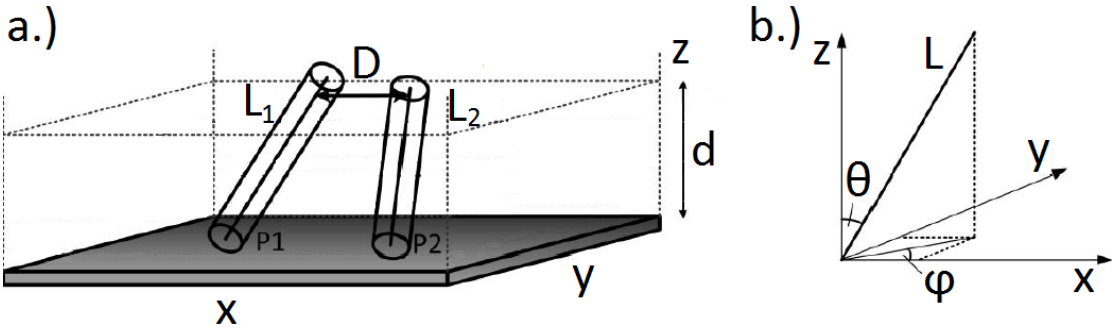

Figure 33: a.) Schematic representation of the simulation box with two randomly placed cylinders. b.) The spherical polar coordinates of a line segment.

Initially, each protein "arrives" perpendicular to the surface, i.e. $\theta = 0°$, after that, they will tilt nicely ($0.5°$ by step) until they touch another particle or they keep slipping until they reach a certain given angle ($0° \leq \theta \leq 90°$). In the case where the cylinders reach a certain interaction distance, the upper one became activated, the program lifts it up and tries to decline it further along at a bit different angle away from the other filament. This procedure influences the compactness of the layer. The number of times (n) the tempering is completed for each particle and the angles ($\delta\phi$) at which they try to avoid each other are also adjustable. Just those cylinders which did not have overlaps with the previously placed ones could lie down totally onto the surface.

In each simulation the simulation box was divided into several sublayers, and after that the total volume fraction of the cylinders was calculated in the simulation box. Therefore, the volume fraction values were able to be defined in each sublayer. The first goal was to find the independent parameters, the three variables are the interaction distance D, the number of heat ups n and of course the different length distribution $f(x)$.

I wrote the program in Python, so that it uses all available processor cores at the same time for speed maximization. As a result, I can run the simulation at the same time with many different combinations of the main parameters.

6.1 Comparison of the results gained from the SE measurements and the simulations

6.1.1 Morphology of the flagellar filaments

In order to understand the $3D$ morphology of the FF layer, SE measurements were performed. By using the evaluation model discussed in section 4.5 the main goal was to determine the thickness of the layer and the amount of protein in the sublayers. I got the density depth profile of the protein layer by the fitting on the measurements. The profile I obtained in this case, also supported our assumption that the density of the layer decreases from the surface, at the upper part the percentage values are below 0.2% (Fig. 34). The low volume fraction values (about 2% near the surface) were caused by the low flagellin concentration (0.02 mg/ml). Note that if the concentration had been higher, the adsorbed amount would have been increased, the higher concentration also would have been caused several overlaps.

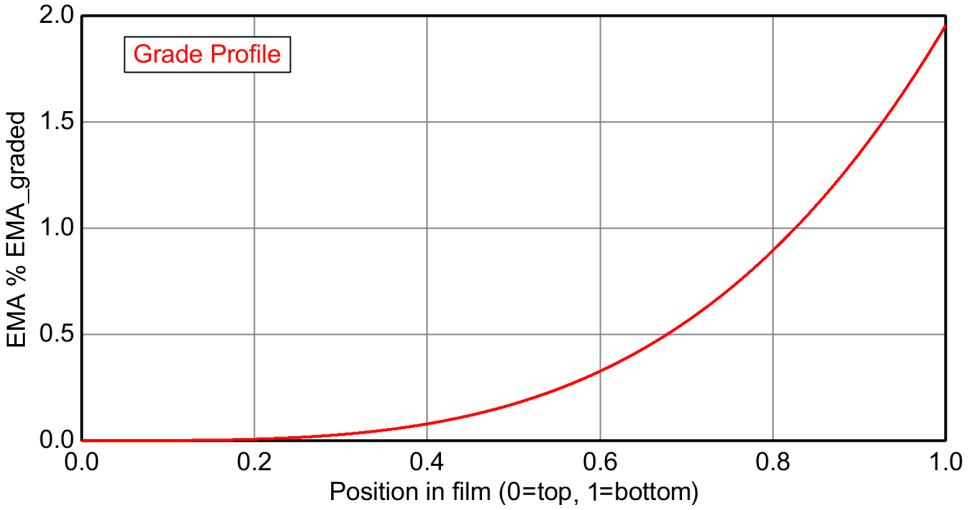

Figure 34: A density-depth profile gained from the SE measurement in the case of 0.02 mg/ml FF concentration.

In this section, I would also like to present the results from three completely different simulations. In the following three models, I used Gaussian distribution for particle sizes. At the end of the first simulation, all the particles could only be perpendicular to the surface, i.e. $\theta = 0°$. In contrast, θ was not secured in the second and third models, and could be in any of the above-mentioned ranges within the aforementioned range. In the third model, most proteins were near the

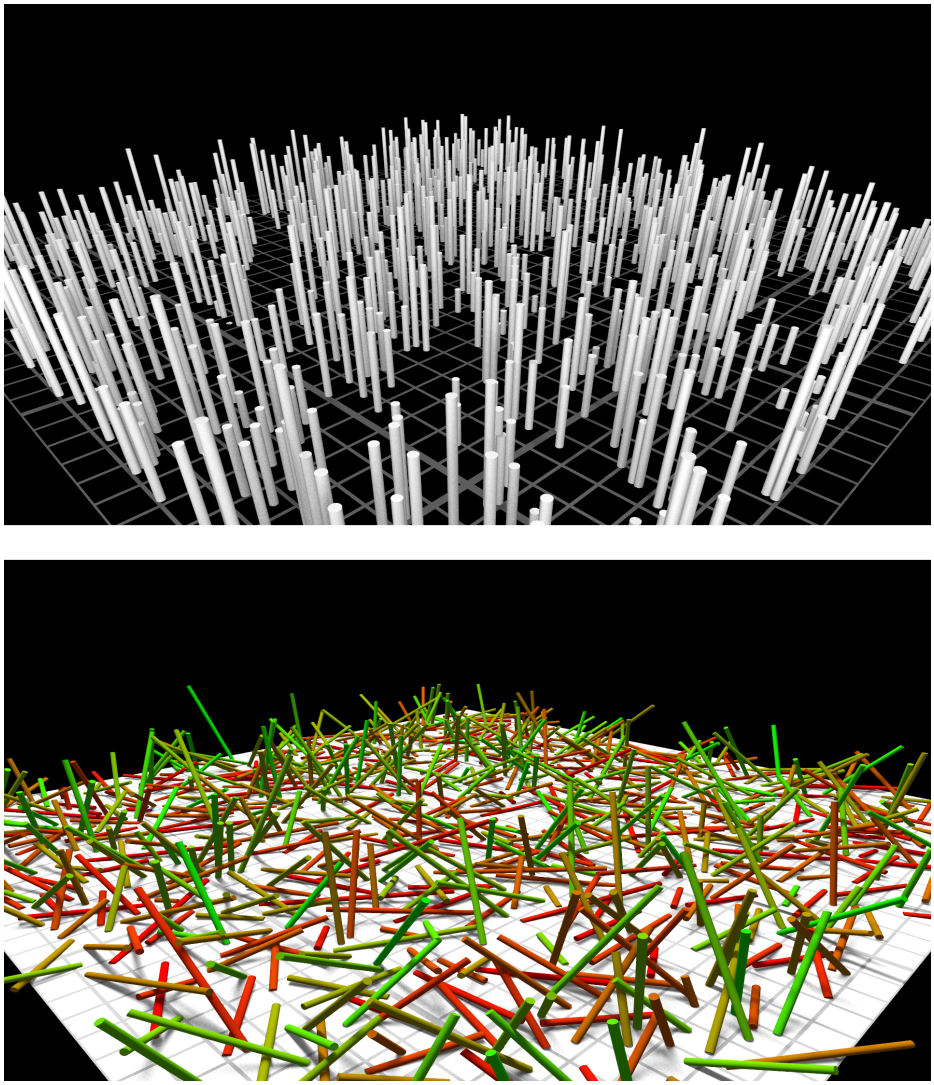

Figure 35: $3D$ morphologies of adsorbed cylinders resulted from the numerical simulation in the case of the 1st and 3rd models.

surface ($\theta \sim 70°$). The second model became an intermediate, as in it, the situation between the two extreme situations can be observed in Fig. 35 and Fig. 36. The pictures were created by the POV-Ray program, the executed C++ like source code was created by my Python code.

As I described above, the cylinders were randomly scattered to the surface one by one, of course, only after examining the overlap exclusion. Then each cylinder was tried to be tilted. So, proteins in large numbers can only lie on the surface if they did not get into the other fallen proteins. This can be controlled by two factors. On the one hand, by applying low concentration of the particles (so there is

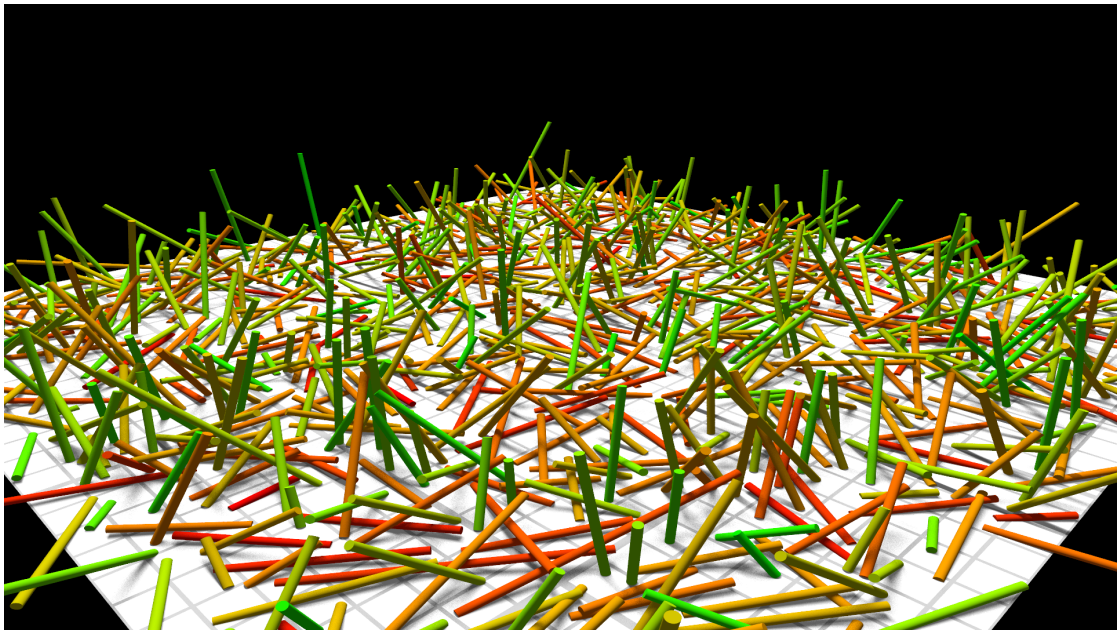

Figure 36: $3D$ morphology of adsorbed cylinders resulted from the numerical simulation in the case of the 2nd model.

little chance of overlaps and jams). On the other hand, by increasing the number of heatups, so that eventually previously deposited flagellins get avoided; in the latter case we get a compact layer close to the surface.

Figure 37 shows that the second model is the most similar to the density profile obtained from the ellipsometric measurement. From this result and many other simulations I concluded that proteins may be on the surface in such a configuration. The next step was to make a link between the calculated protein distribution from the simulation and from the SE measurements. This fit can be done for each measurement. For example the results for the 0.5 mg/ml concentration are shown in Table 1. By knowing the refrective indexes of the FFs and the PBS and the value of dn/dc the adsorbed amount values of the FFs can be calculated [42].

SE (0.5 mg/ml)	d [nm]	100	200	300	400	500
	volume [%]	1.353	0.556	0.169	0.022	0.007
RSA simulation	d [nm]	100	200	300	400	500
	volume [%]	1.396	0.522	0.151	0.019	0.004

Table 1: The comparison of the results gained from SE measurement and RSA simulation.

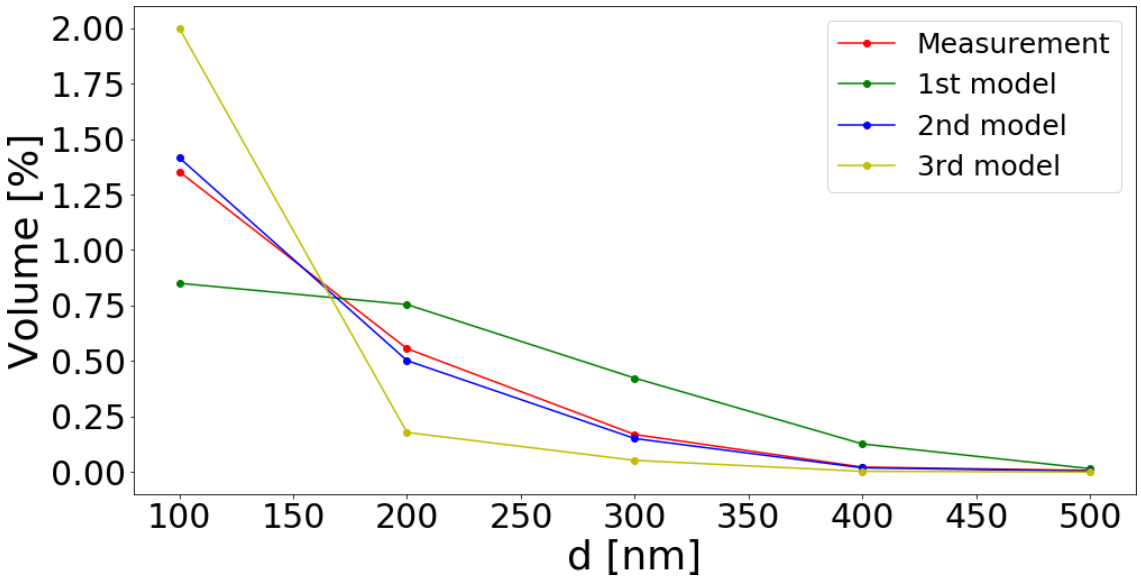

Figure 37: Density-depth profile gained from SE measurement (0.5 mg/ml FF concentration) and profiles resulted from the three different simulation models in cases of 5 sublayers.

It is worth to note that, the used protein length distribution and the other physical and chemical parameters of the substrate or the particles may change the layer's morphology. The substrate can be slightly different, or the surfaces can be hydrophobic and hydrophilic and even chemically modified.

6.1.2 Kinetics of the adsorption

From the simulation we can not only obtain a final three-dimensional structure, but also the kinetics of the structure formation. This kinetics can be compared to the adsorption kinetics of FFs at the solid/liquid interface. I continued to compare the measurements at 0.02 mg/ml concentration with the results from the simulation. In Fig. 34 it can be seen, that in the simulation the protein layer can be broken down into any number of the layers. The kinetics for the proteins in these layers can be individually examined. Of course, the protein volume fraction formed in the whole layer can also be determined.

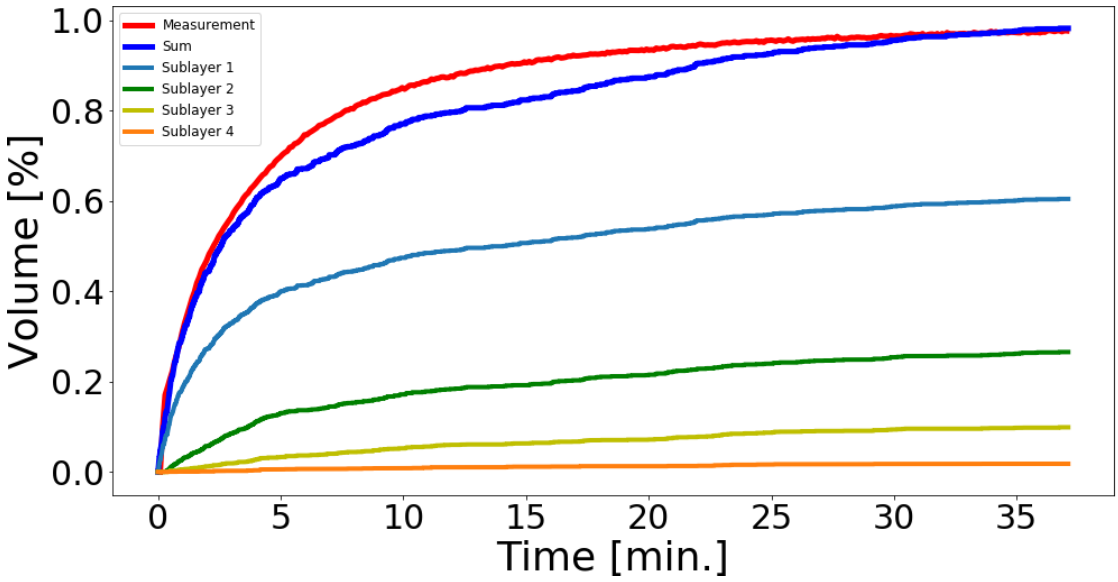

Figure 38: Total adsorbed amount of FF calculated in the EMA (0.02 mg/ml concentration) and volume fraction values as a function of time in each sublayer and their sums resulted from the simulation.

It can also be seen that the obtained kinetics are very similar. With the appropriate parameter settings (above mentioned parameters), the kinetics got from the ellipsometry can be even better approached from the simulation side. From this, I make a conclusion, that the simulation I have written and the parameters set by it, model well the phenomena during the adsorption.

A new program is being written by me, that will be able to find the best simulation result that is appropriate to the given measurement and best describes it by using the functions described in section 5.2. I would like to use the correlations from these to further understand the adsorption of filaments.

Different concentrations of solutions can be used during the measurement. The concentration does not change the result obtained, if we wait long enough, but the kinetics are drastically altered. At higher level of concentrations, surface saturation can be achieved much faster and the functions that describes the measured curve differs. The next step to further improve the simulation will be to shed the concentration dependence. By eliminating this, interaction distances and other new results can be obtained by comparing the simulation and the measurements on the higher level.

6.2 Development of flagellar filament layer modeling

I assumed that by using the stratification structure obtained from the simulation, not only the *3D* structure can be obtained, but it is also possible to achieve new and better results in the evaluation of the measurement. To do this, I tried to fit functions to the resulted depth distribution. Of the functions I tried, the sum of two exponential functions gave the best fit (Fig. 39).

$$f(z) = A_1\, e^{-B_1 * z} + A_2\, e^{-B_2 * z}. \tag{49}$$

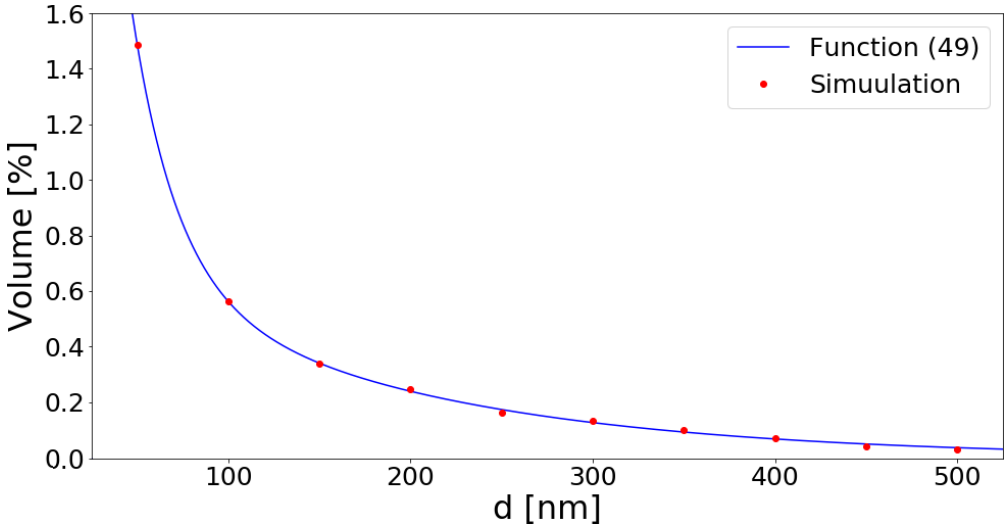

Figure 39: Fit to the density-depth profile gained from the simulation.

In the *CompleteEASE* evaluation program, the grading of the layer can be set not only as exponential, but also as linear or as other functions of the percentage distribution of components. Other options include creating your own equations. The program already has its own stuffed functions. One of them is *isPositive*(), which means that the percentage protein values are always zero or positive, so you can get a physically correct result.

Using the model written in section 4.5 and combining the above-mentioned possibilities, I have created a newer and better model. In which also the main protein layer was 500 nm thick and divided it into 10 sub-layers for easier comparison. The main difference was that the percent values in the layer could not go below zero and that the gradient change was described by two exponential functions (Fig. 40). The simulation has played a very important role in determining the initial values

that must be set in the $f(x)$ function (49). The goodness of my simulation is also shown by the fact that the parameters obtained from it do not deviate much from the right parameter values got from the model.

Graded Layer EMA_kozel Thickness = 500.00 nm
Grade Type = Parametric # of Slices = 10
Profile = Custom
Material = EMA_graded

Name	Equation
EMA	isPositive([value]*([A1]*exp([B1]*[pos])+[A2]*exp([B2]*[pos])),[value]*([A1]*exp([B1]*[pos])+[A2]*exp([B2]*[pos])),0)

Custom Grade Fit Parameters
A1 = 0.01453 (fit) B1 = 5.04062 (fit) A2 = 0.01000 (fit)
B2 = 0.31000 (fit)

Figure 40: New graded EMA layer for flagellar filaments (at 0.02 mg/ml FF concentration).

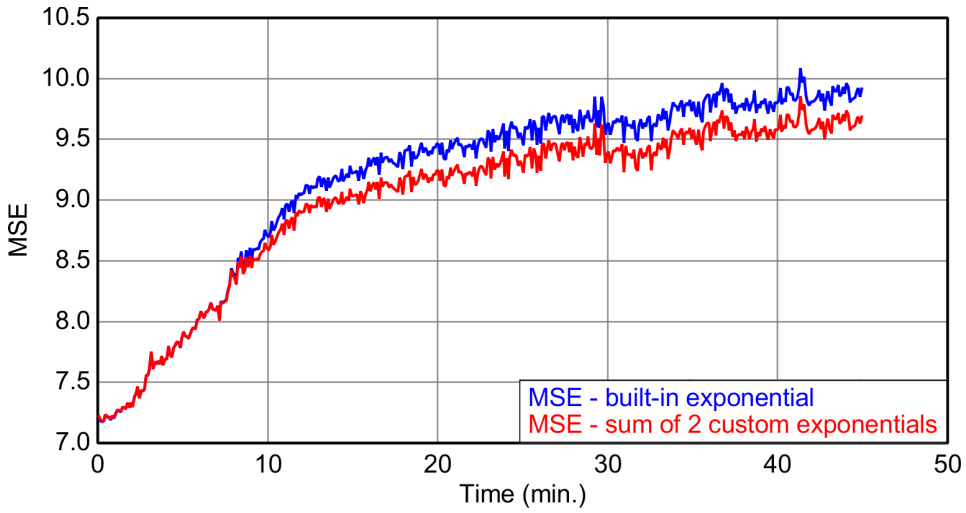

Figure 41: MSE values of graded EMA layer with built-in exponential and of custom graded EMA layer.

Compared to the best exponentially graded model and this new model can be seen to have achieved even better MSE. It follows that this model describes best emerging flagellar filament layer and the kinetics of its formation (Fig. 41). It can be seen that the MSE values will only begin to deviate after 7.5 minutes (the starting point of the protein adsorption) as the deviation in the models differs in the description of the depth-density profiles of the proteins. With the creation of a new well-functioning model, we have achieved the desired goal to create a simple but most applicable analytical method.

7 Összefoglaló

Felületi nanoszerkezetek modellezése szenzorikához

Romanenko Alekszej, Anyagtudomány mesterszakos hallgató
Készült: MTA EK Műszaki Fizikai és Anyagtudományi Intézetén

Témavezető: **Dr. Petrik Péter**, MTA doktora
MTA EK MFA

Fő céljaim közé tartozott, hogy jól használható optikai modellt hozzak létre az új kétcsatornás Kretschmann spektroszkópiai ellipszometriához (SE), és hogy további információkat gyűjtsek az adszorbeált flagelláris filamentumok (FF) morfológiájáról. Ehhez modell fehérjeként fibrinogén (Fgn) adszorpcióját vizsgáltam folyadékcellában. A Fgn és a FF réteg vastagságának, törésmutatójának és tömörségének meghatározása leválasztás közben végzett ellipszometriai mérések segítségével történt, különböző koncentrációk mellett. Kiegészítésként atomi erőmikroszkópia (AFM) eredményeit is használtam. Az AFM mérések alapján meghatároztam filamentumok hosszúság eloszlását, melyet felhasználtam az elkészült szimulációban.

Tanulmányoztam a Fgn-t és a FF-t, hogy megértsem azok szerkezetét és tulajdonságait. A numerikus szimulációba ezeket az adatokat beépítettem. A szimuláció és a kísérleti eredmények közötti konzisztencia azt jelenti, hogy az alkalmazott numerikus model képes jól leírni az adszorbeált FF rétegképződés mechanizmusát. A POV-Ray számára írt program segítségével a szimulált részecskék könnyen láthatóvá és tesztelhetővé váltak.

Emellett sikerült három különböző jól működő modellt létrehoznom az új folyadékcellában való méréshez, melyek közül kettőt ebben a diplomamunkában be is mutattam. Az AFM, SE mérések és a szimuláció közötti összhang jó bizonyítéka az új effektív közeg-közelítésű (EMA) modellek alkalmazhatóságának, ennek segítségével fontos következtetéseket tudtam levonni a FF-ok térbeli struktúrájára.

A kitűzött feladatok közül az egyik megoldása még folyamatban van. A program, amely képes megtalálni a legjobban illeszkedő szimulációt az adott mérésekhez, elkészítése és tesztelése még zajlik.

Összefoglalva elmondható, hogy sikeresen elértem kutatási célomat, hogy elősegítsem a FF alapú bioszenzor kifejlesztését. Az elvégzett kutatásból két publikáció megjelentetését tervezzük.

8 Summary

Modeling of surface nanostructures for sensorics

Alekszej Romanenko, MSc student in Materials Sciencey
Place of diploma work: MTA EK MFA, Budapest

Supervisor: **Dr. Péter Petrik**, DSc
MTA EK MFA

The primary goal was to gather more information about the morphology of the adsorbed flagellar filaments (FFs) by using the Kretschmann setup for spectroscopic ellipsometry (SE). To do so, I investigated the adsorption of a model protein - fibrinogen (Fgn) in flow cell. Determination of the thickness and compactness of the Fgn and FF layers formed during the adsorption was achieved by SE measurements at different concentrations. In addition, the results of an alternative method - atomic force microscopy (AFM) were used to support the results, this measurements were also used to determine the length distribution of the filaments.

I thoroughly reviewed the Fgn and FF to get acquainted with their structure, their properties, and of course the scales. This information were used in the simulation. The consistency between numerical and experimental results implies, that the applied numerical simulation can well describe the mechanisms of the adsorbed FF layer formation. With this simulation I could draw conclusions about the spatial position of the particles. Further options include adding the concentration as parameter into the simulation, thus achieving even more accurate results.

In addition, I managed to create three different well-functioning models for the new compilation, two of them were described in this thesis in more details. Usage of the graded layer is common in ellipsometric evaluations, but its usage for modeling protein layers is an innovation. The agreement between the SE, AFM measurements and the simulation is a good proof of the applicability of the graded effective medium approximation (EMA) model and it gives detailed information about the assumed orientation of the FFs.

One of the goals set has not yet been achieved - the program, that will be able to find the best fitting simulation results to the given measurements. However the preparations and testings are underway. In summary, I have successfully achieved my research goal, to assist the development of a flagellar filament based biosensors. In addition, two publications will be made on the base of this work.

9 Future work

On the one hand, one of my further goals is to stabilize all external factors (e.g. temperature) during the data gathering to improve the measurements to get an accurate picture of the FF receptor layer. The required temperature stabilizer cell (that can stabilize the temperature from 20° to 60°) will be ready soon.

On the other hand, the new program's testing and writing is about to be completed soon. I would like to use the received correlations between the measurement and simulations to better understand the physics behind the adsorption kinetics. To do so I would like to eliminate the concentration factor from the process by adding it as a parameter to my simulation.

In the recent days we have carried out a successful experiment with a sensor chip covered by the protein layer modified by the nickel detection bonds. The next steps will be the development of further chips that are capable to detect even smaller concentration of Ni atoms and, secondly, the development of a sensors for other molecules or atoms (e.g. arsenic). Therefore we are on the threshold of creating a new type of biosensor.

References

[1] K. K. Jain, Nanotechnology in clinical laboratory diagnostics, *Clinica Chimica Acta*. vol. 358, pp. 37–54, (2005).

[2] K. Tiefenthaler and W. Lukosz, Grating couplers as integrated optical humidity and gas sensors, *Thin Solid Films*, vol. 126, pp. 205–211, (1985).

[3] W. Lukosz, Integrated optical chemical and direct biochemical sensors, *Sensors and Actuators*, vol. 29, pp. 37–50, (1995).

[4] J. Vörös, J. Ramsden, G. Csúcs, I. Szendrő, S. D. Paul, M. Textor, and N. Spencer, Optical grating coupler biosensors, *Biomaterials*, vol. 23, pp. 3699–3710, (2002).

[5] R. Horvath, H. Pedersen, N. Skivesen, D. Selmeczi, and N. Larsen, Optical waveguide sensor for on-line monitoring of bacteria, *Optics Letters*, vol. 28, pp. 1233–1235, (2003).

[6] J. P. Chambers, B. P. Arulanandam, L. L. Matta, A.Weis, and J. J. Valdes, Biosensor recognition elements, *Current Issues in Molecular Biology*, vol. 10, pp. 1–12, (2008).

[7] N. Trummer, N. Adányi, M. Váradi, and I. Szendrö, Modification of the surface of integrated optical waveguide sensors for immunosensor applications, *Fresenius J. Anal. Chem.* 371(1), 21–24 (2001).

[8] S. Kurunczi, R. Horvath, Y. P. Yeh, A. Muskotál, A. Sebestyén, F. Vonderviszt, and J. J. Ramsden, Selfassembly of rodlike receptors from bulk solution, *J. Chem. Phys.* 130(1), 011101 (2009).

[9] D. Patko, K. Cottier, A. Hamori, and R. Horvath, Single beam grating coupled interferometry: high resolution miniaturized label-free sensor for plate based parallel screening, *Opt. Express* 20(21), 23162–23173 (2012).

[10] J. Vörös, The density and refractive index of adsorbing protein layers, *Biophys. J.* 87(1), 553–561 (2004).

[11] H. Fujiwara, Spectroscopic Ellipsometry: Principles and Applications *John Wiley & Sons*, Ltd, (2007).

[12] A. Nemeth, P. Kozma, T. Hülber, S. Kurunczi, R. Horvath, P. Petrik, A. Muskotál, F. Vonderviszt, C. Hős, M. Fried, J. Gyulai, and I. Bársony, In Situ Spectroscopic Ellipsometry Study of Protein Immobilization on Different Substrates Using Liquid Cells, *Sens.* Lett. 8(5), 730–735 (2010).

[13] *https://www.jawoollam.com/resources/ellipsometry-tutorial*

[14] H. Arwin, Polarized Light and Ellipsometry, (Handbook of Ellipsometry, H. G. Tompkins, E. A. Irene), NY, (2005).

[15] T. Mosoni, P. Petrik, M. Fried, I. Barsony, Modular, PC controlled photometric ellipsometer with variable angle of incidence and spectral options, *SPIE Proceedings* 3573, 355 (1998).

[16] M. Born, E. Wolf, Principles of optics. *Pergamon Press*, London, (1968).

[17] J. Nádor, B. Kalas, A. Saftics, E. Ágocs, P. Kozma, L. Kőrösi, I. Szekacs, M. Fried, R. Horváth, P. Petrik, Plasmon-enhanced two-channel in situ Kretschmann ellipsometry of protein adsorption, cellular adhesion, and polyelectrolyte deposition on titania nanostructures, *Opt Express* 24 4812–4823 (2016).

[18] P. Drude, Oberflächenschichten, *Ann. Phys. Chem.*, 36, 532 (1889).

[19] P. Drude, Oberflächenschichten, *Ann. Phys. Chem.*, 36, 865 (1889).

[20] É. Kiss, Characterization of Polymer Blends: Ellipsometry In: Thomas Sabu, Grohens Yves, Jyotishkumar P. (eds.) Characterization of Polymer Blends: Miscibility, Morphology and Interfaces ISBN 978-3-527-33153-6 - *Wiley-VCH, Weinheim* chp. 9. pp. 299-326, (2014)

[21] J. A. De Feijter, J. Benjamins, and F. A. Veer, Ellipsometry as a tool to study the adsorption behavior of synthetic and biopolymers at the airwater interface, *Unilever Research*, 1759 (1977).

[22] *http://www.microworldreflections.com/atomic-force-microscopy.html*

[23] J. L. Orgtega-Vinuessa, P. Tengval, I. Lundstrom, Molecular packing of HSA, IgG, and fibrinogen adsorbed on silicon by AFM imaging. *Thin Solid Films* 324, 257-273 (1998).

[24] A. K. Bajpai, Fibrinogen adsorption onto macroporous polymeric surfaces: correlation with biocompatibility aspects. *Springer Science*, (2007).

[25] H. C. F. Côté, S. T. Lord, K. P. Pratt, γ-Chain Dysfibrinogenemias: Molecular Structure-Function Relationships of Naturally Occurring Mutations in the γ Chain of Human Fibrinogen, *Blood*, 92:2195-2212, (1998).

[26] C. G. Gölander, É Kiss, Protein adsorption on functionalized and ESCA-characterized polymer films studied by ellipsometry. *Journal of Colloid and Interface Science*, 121(1), 240-253. DOI: 10.1016/0021-9797(88)90428-6, (1988).

[27] F. A. Samatey, K. Imada, S. Nagasima, F. Vonderviszt, T.Kumasaka, M. Yamamoto,and K. Namba, Structure of the bacterial flagellar protofilament and implications for a switch for supercoiling, *Nature*, vol. 410, pp. 331–337, (2001).

[28] F. Vonderviszt, H. Uedaira, S. Kidokoro, and K. Namba, Structural organization of flagellin, *Journal of Molecular Biology*, vol. 214, pp. 97–104, (1990).

[29] K. Namba and F. Vonderviszt, Molecular architecture of bacterial flagellum, *Quarterly Review of Biophysics*, vol. 30, pp. 1–65, (1997).

[30] I. Yamashita, K. Hasegawa, H. Suzuki, F. Vonderviszt, Y. Mimori-Kiyosue, and K. Namba, Structure and switching of bacterial flagellar filaments studied by x-ray fiber diffraction, *Nature Structural Biology*, vol. 5, pp. 125–132, (1998).

[31] K. Namba K, F. Vonderviszt, Molecular architecture of bacterial flagellum. *Quarterly Review of Biophysics*, 30, 1-65 (1997).

[32] K. Yonekura, S. Maki-Yonekura, and K. Namba, Complete atomic modell of the bacterial flagellar filament by electron cryomicroscopy, *Nature*, vol. 424, pp. 643–650, (2003).

[33] A. Muskotál, Cs. Seregélyes, A. Sebestyén, F. Vonderviszt, Structural Basis for Stabilization of the Hypervariable D3 Domain of Salmonella Flagellin upon Filament Formation. *Journal of Molecular Biology.* 403, 607–615 (2010).

[34] V. Szabó, A. Muskotál,B. Tóth et al., Construction of a Xylanase a Variant Capable of Polymerization. PLOS ONE. 6, E25388 (2011).

[35] P. Kozma, D. Kozma, A. Nemeth, H. Jankovics, S. Kurunczi, R. Horvath, F. Vonderviszt, M. Fried, P. Petrik, *Applied Surface Science* 257 7160–7166 (2011).

[36] *http://alag3.mfa.kfki.hu/mfa/nyariiskola/11_Ellipszometria/index.htm*

[37] M. Poksinski and H. Arwin, Protein monolayers monitored by internal reflection ellipsometry, *Thin Solid Films* 455–456, 716–721 (2004).

[38] T. W. H. Oates, H. Wormeester, and H. Arwin, Characterization of plasmonic effects in thin films and metamaterials using spectroscopic ellipsometry, *Prog. Surf. Sci.* 86(11-12), 328–376 (2011).

[39] K. Hinrichs, K.-J. Eichhorn (Eds.), Ellipsometry of Functional Organic Surfaces and Films, *Heidelberg*, (2014.)

[40] M. Poksinski, H. Arwin, in: *Thin Solid Films*, volume 455-456, pp. 716–721.

[41] B. Kalas, J. Nádor, E. Agócs, A. Saftics, S. Kurunczi, M. Fried, P. Petrik, Protein adsorption monitored by plasmon-enhanced semi-cylindrical Kretschmann ellipsometry. *Applied surface science*, 421. pp. 585-592. ISSN 0169-4332 (2017).

[42] L. G. Castro, D. W. Thompson, T. Tiwald, E. M. Berberov, and J. A. Woollam, Repeatability of ellipsometric data in cholera toxin gM1-elisa structures. *Surface Science*, 601:1795, (2007).

[43] M. A. Brusatori, Dissertation: Protein adsorption kinetics under an applied electric field: an Optical Waveguide Lightmode Spectroscopy study, *Graduate School of Wayne State University, Detroit, Michigan*, (2001).

[44] J. J. Ramsden, From Kinetics to Structure: High Resolution Molecular Microscopy Proteins, *Solid-Liquid interfaces*, (2006).

[45] *http://www.lrg.rice.edu/Content.aspx?id=33*

[46] J. Talbot, G. Tarjus, P. R. Van Tassel, P. Viot, From Car parking to Protein Adsorption: An Overview of Sequential Adsorption Processes, Condensed Matter, Statistical Mechanics, (1999).

[47] P. Viot, G. Tarjus, S.M. Ricci, J. Talbot, Random sequential adsorption of anisotropic particles. I. Jamming limit and asymptotic behavior. *Journal of Chemical Physics* 97, (1992).

[48] J. F. Douglas, H. M. Schneider M. Schneider, P. Frantz, R. Lipman, S. Granick, The origin and characterization of conformational heterogeneity in adsorbed polymer layers, *Journal of Physics Condensed Matter*, (1999).

[49] Y. Tie, C. Calonder, P. R. Van Tassel, Protein adsorption: Kinetics and history dependence, *Journal of Colloid and Interface Science*, 268, 1–11 (2003).

Nyilatkozat

Név: Romanenko Alekszej
ELTE, Természettudományi kar, szak: Anyagtudomány MSc.
Neptun azonosító: YGH8TE
Szakdolgozat címe: Modeling of surface nanostructures for sensorics

A **szakdolgozat** szerzőjeként fegyelmi felelősségem tudatában kijelentem, hogy a dolgozatom önálló munkám eredménye, saját szellemi termékem, abban a hivatkozások és idézések standard szabályait következetesen alkalmaztam, mások által írt részeket a megfelelő idézés nélkül nem használtam fel.

Budapest, 2017.12.28

a hallgató aláírása

Declaration of Authorship

Name: Alekszej Romanenko
ELTE, Faculty of Science: Materials Science MSc.
Neptun code: YGH8TE
Thesis title: Modeling of surface nanostructures for sensorics

As the author of this **thesis**, I declare, with my disciplinary responsibility, that my work is the result of my own work, it is my own intellectual product, the references and summaries follow the standard rules, and I have not used any other parts written by others without proper summons.

Budapest, 28 December, 2017

signature of the student